

Implantable Energy Harvesting Stents for Transcutaneous Wireless Monitoring of Peripheral Artery Disease

Michael A. Rothfuss Nicholas G. Franconi Kara N. Bocan Jignesh V. Unadkat Michael L. Gimbel Marlin H. Mickle Ervin Sejdić

Abstract—More than 5 million adults in the US are affected by peripheral artery disease. Current wireless stent monitors are unsuitable for use in the thigh. In this paper, wireless powering and communication with implanted stents were investigated. Specifically, we investigated the effects of thigh tissue morphology and tissue thickness variations on wireless power gain and electromagnetic safety when using skin-contact touch probe antennas. Thigh simulation models were derived from anthropometric data for the diseased population. Power gain and specific absorption rate were determined for each variation. To corroborate human model simulation results, a power-to-frequency converter was designed, benchmarked, and implanted within *ex vivo* porcine tissue. The experiments showed the most realistic simulations reported so far that have the best agreement with measured results. This work indicates that touch probe powered stent systems can safely deliver significant power to an implant. This research enables frequent at-home monitoring to replace costly in-hospital quarterly check-ups.

Keywords: Biomedical monitoring, implantable biomedical telemetry, implantable biomedical devices, peripheral arterial disease, stent, touch probe, wireless power

I. INTRODUCTION

Atherosclerosis is a disease described by the accumulation of plaque in arterial walls, which restricts or obstructs blood flow to organs, limbs, etc., depending on the disease location. Heart attack, stroke, limb amputation, and even death are potential consequences of atherosclerosis [1], [2]. When this disease affects arteries in the lower-limbs, it is called peripheral artery disease (PAD) [3]. In the US, PAD affects in excess of 5 million adults. The aging population shows a higher prevalence for the disease, with 4.3% adults aged 40 years or more in the United states affected. Increasing age correlates to significantly higher incidence: 0.9% of adults aged 40 – 49 years, 2.5% of adults aged 50 – 59 years, 4.7% of adults aged 60 – 69 years, and 14.5% of adults over 70 years [4].

A common atherosclerosis surgical intervention technique involves deploying stents within the vessel lumen to reopen

the occluded vessel, thereby resuming blood flow to the surrounding tissue. PAD is typically asymptomatic until its later stages [5], and despite surgical intervention, the likelihood of restenosis results in first-year complications near 50% [6], with 3-year patency at 66% [7]. Patients must follow up with quarterly or biannual hospital visits to detect blockages using imaging studies [8]. Unfortunately, 20 – 50% of patients with restenosis are asymptomatic. It has been established [9] that the absence of symptoms is negatively correlated with patient compliance with follow-up evaluations [10]. Therefore, a large percentage of patients that redevelop the disease go undetected until too late. The prevalence of stents in the upper body (e.g., carotid [11], coronary [12], etc.) has lead to the development of many “smart stents” that wirelessly telemeter the degree of restenosis. Wireless reporting stands to rapidly detect plaque proliferation by replacing the quarterly in-hospital visits with frequent at-home monitoring.

Prior studies fit into two general categories: detecting plaque proliferation and characterizing the wireless stent link in various tissue models. While a couple studies investigated plaque growth from the standpoint of tissue dielectric properties [13], [14], [15], the most prevalent technique found in literature incorporated capacitive pressure sensors for intraluminal blood pressure changes [16], [17], [18], [19], [20]. Blood pressure sensing within the stent lumen provides valuable information for cardiac health.

However, pressure measurement within the stent is less suited for peripheral vascular monitoring, as the ratio of blood pressure at the ankle and arm is more instructive for diagnosis than pressure measurement within the stent [21]). Conversely, blood flow velocity at the stent site is directly related to stenosis degree, and represents a more important stent-based metric for the diagnosis of disease [22]. Therefore, it would be advantageous from a clinical point of view to wirelessly interrogate stents used to monitor PAD. Studies investigating the wireless links sought to compare tissue models (e.g., simulation, saline, *ex vivo*, etc.) with *in vivo* animal experiments [23], [24], [25]. Model accuracy varies widely, mostly due to measurement technique [26] and the morphological differences between the models and animals [23], [24]. Available *in vivo* animal studies use a porcine animal model [23], [24], [18] whose tissues are more electromagnetically similar to a young child, rather than an adult [27]. Thereby, highlighting an additional source of model-animal accuracy disagreement not previously considered. Moreover, the safety of wireless stent

Michael A. Rothfuss, Nicholas G. Franconi, Kara N. Bocan, Marlin H. Mickle, and Ervin Sejdić are with the Department of Electrical and Computer Engineering, Swanson School of Engineering, University of Pittsburgh, Pittsburgh, PA, USA. E-mails: mar28@pitt.edu, ngf3@pitt.edu, knb12@pitt.edu, mickle@pitt.edu, esejdic@ieee.org

Jignesh V. Unadkat and Michael L. Gimbel are with the Department of Plastic Surgery, University of Pittsburgh, Pittsburgh, PA, USA. E-mails: unadkatjv@upmc.edu, gimbelml@upmc.edu.

systems is largely unknown and seldom considered [18], [25], despite being a major barrier towards commercial adoption.

In this study, we demonstrate a wireless monitor that can be used to safely monitor PAD, reducing the need for limb amputation and the potential for heart attack and stroke. We develop anthropometric-data driven simulation models for the representative aging PAD population and a common lesion location in the superficial femoral artery. We investigate the wireless link accuracy in *ex vivo* porcine simulations and measurements to confirm our approach to tissue and implant location modeling. Safety limits are investigated using various touch probe antennas for power delivery to shallow and deep implants. From our work, we provide a basis of understanding wireless PAD monitoring in humans. Using this technology, PAD could be monitored at home to catch lesion growth before it reaches an advanced state, and it would eliminate the need for patients to make hospital visits every few months. Determining the available power that can be safely delivered to the implant opens the field to incorporating power hungry piezoelectric Doppler transducers. The Doppler transducers would provide the familiar intraluminal Doppler blood flow sonogram currently used by clinicians to measure lesion severity.

II. MATERIALS AND METHODS

The finite element solver HFSS (ANSYS, Pittsburgh, PA, USA) was used to model and simulate the 3-D anthropometric model along with the implanted stent antenna and external touch probe. HFSS models and results were co-simulated using ANSYS Designer before data extraction for analysis. Additionally, the SPICE simulator, LTSpice IV (Linear Technology, Milpitas, CA, USA) was used to simulate the overall system, including the implanted electronics, external electronics, and tissue/antenna models. Lumped element equivalent models of the human thigh and antennas were derived from the HFSS results and used in LTSpice for a full system simulation. The 3-D model of the human thigh tissues, including vasculature, plaque, and bone, as well as the stent antennas and touch probe antenna are shown in Figure 1. The following sub-sections develop the model shown in this figure. Finally, porcine tissue is used to experimentally verify the simulated models.

A. Deriving Anthropometric Simulation Models

Simulation tissue thickness ranges were taken from data published for the aging population, due to PAD's prevalence in this group. Because the correlation between obesity and PAD depends on the metric used (i.e., body mass index, waist circumference, waist-to-thigh ratio, etc.) [28], we studied a range of fat thicknesses. Additionally, the connection between diabetes and PAD has been confirmed through epidemiological data [29], and therefore, anthropometric data for diabetics was also considered.

The thigh is geometrically modeled as a layered model, which simplifies the simulation complexity. The layered model was shown by Lin et al. to be the best candidate for modeling an implant location [30], compared with rectangular and

circular geometric models. Detailed derivations of the anthropometric values are found in the Supplementary Material. A summary of all derived anthropometric values are presented in Table I.

B. Touch Probe Simulation Model

The external antenna is a touch probe antenna. The touch probe antenna makes direct contact with skin. The design used in this research was designed to operate in the mid- to low-hundreds of MHz, and is based on Liu et al.'s design at 915 MHz [33], [34]. The touch probe in this work uses planar rectangular electrodes, rather than the thick and rounded-edges used by Liu et al. The trace and electrode thickness were increased slightly above the manufactured thickness (i.e., 43.18 μm compared to 215.9 μm) to reduce the large aspect ratio between trace thickness and the surrounding geometries in the simulation model. Because Liu et al. showed that power gain to the implant is maximized when the electrodes' width equals the electrode separation, the electrode length and width are both fixed at 3 cm for human model simulations. The PCB extends 0.5 cm around the electrodes' edges. The touch probe antenna uses an SMA connector interface and is fed by a coaxial cable. A 61 material ferrite choke (i.e., PN: 0461164281, Fair-Rite Products Corp., Wallkill, NY, USA) is modeled nearest the side of the touch probe antenna to prevent surface currents on the outside of the coaxial cable, which would undesirably make the coaxial cable part of the antenna.

C. Tissue and Antenna Simulation Set-up and Procedure

Two simulation models were investigated. One is a human model, and the other was an *ex vivo* porcine tissue model for experimental verification, used in lieu of human tissue experiments. That is to say, porcine experiments are compared to only porcine simulations, which serves to validate the human model simulations. The two simulation models are referred to by *Model 1* and *Model 2* throughout this paper, and are described below:

- *Model 1*: The human tissue model using a fixed touch probe size – electrode width and length both equal 3 cm. Fat thickness and vessel location are varied. A variation of Model 1, where electrode separation and width are varied, is used to study SAR. Maximum available gain, G_{MAX} , is used to compare touch probes.
- *Model 2*: The *ex vivo* porcine tissue model using touch probes with varied separation and width. This model is compared to experimental measurements. Implant location, implanted hardware, and tissue thicknesses are modeled closely to the dimensions in the experiments. Simulations and measurements use available gain, G_A .

Both models use a layered stack-up. In *Model 1*, the length and width of the tissue layers approximates a human thigh – 33 cm and 20 cm, respectively. Human tissues' relative permittivity (ϵ_r) and conductivity (σ) were extracted across the simulated bandwidth from an online database [35] and are shown in Table I, along with each material's density.

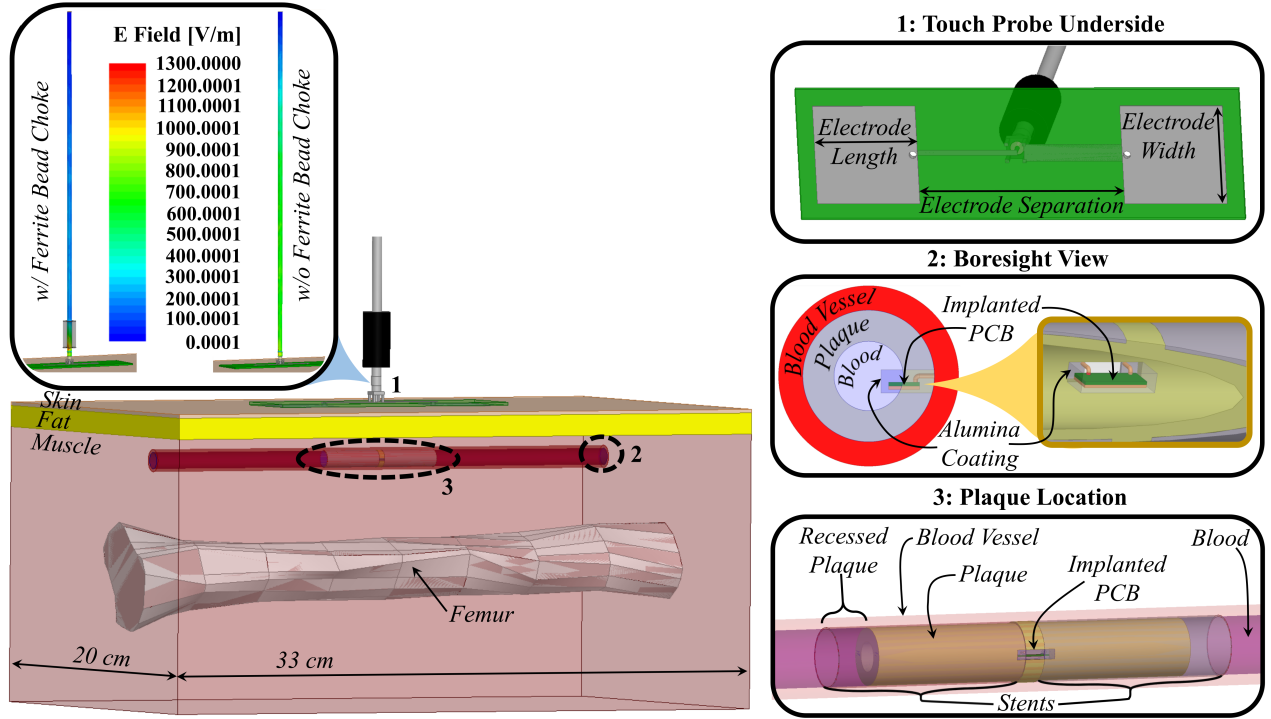


Fig. 1. HFSS 3-D model showing the touch probe antennas, stents as antennas, implanted electronic PCB, layered human thigh model, vasculature, plaque, and blood. Note the use of a ferrite choke to reduce currents on the coaxial shield outer side.

TABLE I

SUMMARY OF SIMULATION MODEL MATERIALS AND PARAMETERS. “*” DENOTES MULTIPLICATION BY 10^{-2} AND “†” DENOTES MULTIPLICATION BY 10^{-1} . BLOOD VESSEL DENSITY OBTAINED FROM MIAO ET AL. [31]; ALL OTHER DENSITIES FROM RAHMAT-SAMII AND KIM [32].

Material / Parameter	Thickness (mm)	Increment (mm)	ϵ_r (100 → 500 MHz)	σ (S/m) (100 → 500 MHz)	Density (kg/m ³)
blood	—	—	76.8 – 63.3	1.23 – 1.38	1060
blood vessel	1.35	—	59.8 – 46.2	4.62 – 5.86 [†]	1100
cortical bone	15.0 (mid-shaft radius)	—	15.3 – 12.9	6.43 – 10.0*	1810
fat	1.00 – 31.0	10	6.07 – 5.54	3.63 – 4.28*	920
muscle	56.0	—	66.0 – 56.4	7.08 – 8.22 [†]	1040
plaque	0.00 – 4.50	2.25	same as fat	same as fat	same as fat
skin (wet)	1.90	—	66.0 – 48.6	5.23 – 7.04 [†]	1010
electrode separation	10.0 – 60.0	10			
vessel location	8.70 – 20.7	3			

The relative permeability for tissues is near the free space permeability [36] and therefore set to one [37], [38], [39].

The scattering parameters (S-parameters) of the simulated models were extracted from HFSS/Designer across a frequency sweep range of 100 – 500 MHz to capture the peak power gain. The approximate center of this sweep range corresponds to the preferred far-field operational frequency of the 60 mm implanted dipole in muscle tissue. Specifically, 308 MHz corresponds to exactly a 120 mm wavelength in muscle. The close proximity of the stent antenna and the touch probe means near-field effects are expected, necessitating this wideband sweep to capture the peak power gain.

For *Model 1*, the maximum available gain, G_{MAX} , is calculated to compare touch probe antennas against one another. G_{MAX} assumes that the network ports are simultaneously

conjugately matched. From Pozar [40], G_{MAX} is calculated using Eq. (1):

$$G_{MAX} = \frac{1}{1 - |\Gamma_S|^2} |S_{21}|^2 \frac{1 - |\Gamma_L|^2}{|1 - S_{22}\Gamma_L|^2} \quad (1)$$

where Γ_S and Γ_L are the source and load reflection coefficients under simultaneous conjugate matching, respectively, and are calculated using Eq. (2):

$$\Gamma_S = \frac{B_1 \pm \sqrt{B_1^2 - 4|C_1|^2}}{2C_1} \quad (2a)$$

$$\Gamma_L = \frac{B_2 \pm \sqrt{B_2^2 - 4|C_2|^2}}{2C_2} \quad (2b)$$

where:

$$\begin{aligned} B_1 &= 1 + |S_{11}|^2 - |S_{22}|^2 - |\Delta|^2 \\ B_2 &= 1 + |S_{22}|^2 - |S_{11}|^2 - |\Delta|^2 \\ C_1 &= S_{11} - \Delta S_{22}^* \\ C_2 &= S_{22} - \Delta S_{11}^* \\ \Delta &= S_{11}S_{22} - S_{12}S_{21} \end{aligned}$$

where S_{11} , S_{12} , S_{21} , and S_{22} are the extracted S-parameters and $Z_0 = 50 \Omega$, the characteristic impedance of the system. When computing the source and load reflection coefficients, if B_1 and B_2 are greater than 0, the minus sign of the \pm is used in Eq. (2).

SAR is computed for a shallow implant depth at 0% and 100% occlusions to show plaque's effect. Additionally, SAR is computed for a deep implant depth at 0% occlusion to uncover effects for deeper implants. Using *Model 1*, the electrode separation and width are varied from 1 cm – 6 cm. SAR is computed on the skin surface at the air-skin interface, as is done by Moradi et al. [41]. A 1 Watt drive, under a simultaneous impedance matching condition at the two antenna port interfaces, is used for SAR computations. The simultaneous matching condition serves as a basis for comparing the touch probe antennas, regardless of impedance variations at the antenna port interfaces, which would introduce mismatch losses that decreases SAR. To compute the requisite source and load terminating impedances, Z_S and Z_L , respectively, for the simultaneous matching condition, Eq. (3) is calculated from Pozar [40]:

$$Z_S = Z_0 \frac{1 + \Gamma_S}{1 - \Gamma_S} \quad (3a)$$

$$Z_L = Z_0 \frac{1 + \Gamma_L}{1 - \Gamma_L} \quad (3b)$$

where Γ_S and Γ_L are calculated from Eq. (2) and $Z_0 = 50 \Omega$.

Two standards, the IEEE Standard C95.1-2005 [42] and that defined by the International Commission on Non-Ionizing Radiation Protection (ICNIRP) [43], are often quoted for human safety exposure limits to electromagnetic fields. In the thigh, for the 100 – 400 MHz band, the C95.1-2005 standard states a localized exposure limit of 2 W/kg average in a 10 gram tissue volume over 30 minutes, for the general public. The ICNIRP also recommends the 2 W/kg limit in a 10 gram tissue volume but instead over a 6 minute averaging period. Because the computed SAR may exceed regulatory limits, either duty cycling the transmit on-time or reducing the touch probe drive power can be effectively used to meet regulatory limits. To scale the drive power to meet the SAR threshold, the parameter adjusted gain, $G_{adj, SAR}$ is computed using Eq. (4):

$$G_{adj, SAR} = 10 \cdot \log_{10} \left(\frac{2 \text{ W/kg}}{\%T_{on} \cdot \text{SAR}_{10\text{-g}}} \right) \quad (4)$$

where $\text{SAR}_{10\text{-g}}$ is the computed 10 gram peak spatial-average SAR from HFSS/Designer on the skin surface, $\%T_{on}$ is the percent on-time during the SAR averaging time period (i.e., 6 minutes or 30 minutes, depending on the standard used), and

2 W/kg is the 10 gram peak spatial-average SAR limit in both standards. Negative values of adjusted gain correspond to a necessary reduction in the drive power by $G_{adj, SAR}$ to meet the SAR threshold. Likewise, positive $G_{adj, SAR}$ means power can be increased while still meeting SAR regulations.

To facilitate practical measurements in *Model 2*, the touch probe is left unmatched and terminated by the 50Ω coaxial cable feed, while the implanted antenna's terminals were impedance matched to and terminated with the implanted electronics. Impedance matching at the load-side only is described by the available power gain, G_A , shown in Eq. (5) by [40]:

$$G_A = \frac{|S_{21}|^2 (1 - |\Gamma_S|^2)}{|1 - S_{11}\Gamma_S|^2 (1 - |\Gamma_{out}|^2)} \quad (5)$$

where:

$$\begin{aligned} \Gamma_{out} &= S_{22} + \frac{S_{12}S_{21}\Gamma_S}{1 - S_{11}\Gamma_S} \\ \Gamma_S &= \frac{Z_S - Z_0}{Z_S + Z_0} \end{aligned}$$

and Γ_{out} is the reflection coefficient looking away from the load at the two-port network-load interface, Γ_S (i.e., not the same Γ_S found in Eq. (2)) is the reflection coefficient looking towards the source at the source-two-port network interface, and Z_S is the terminating impedance of the source. $Z_0 = 50 \Omega$.

D. Implanted Stent Dipole Antenna, Implant Simulation Models, & Implant Environment

Stents are wire mesh tubes placed within a blood vessel to reintroduce blood flow due to a blockage. Stents act as conduits allowing blood to flow unimpeded through the vessel. Stents are fed into a vessel in a collapsed state using a catheter guide-wire, which sometimes has an inflatable balloon to force the stent into its un-collapsed final state. The stents used in this research are self-expandable (i.e., no balloon) Nitinol Cordis PRECISE PRO RX[®] Carotid stents (from Cordis, Milpitas, CA, USA) measuring 3 cm long with a 0.9 cm outer-diameter. The stent wire mesh wall thickness was measured at 230 μm . The implanted stent antenna is comprised of two stents, where each stent forms an arm of a dipole antenna. A 3 mm gap is used between the two stents dipole arms to facilitate an antenna feed.

Examining the 60 mm stent antenna as a half-wave dipole, its operating frequency is expected to be somewhere near 300 MHz (i.e., 308 MHz has a wavelength of 120 mm in muscle tissue). Because the stent's mesh holes are significantly smaller than the expected operating wavelength in tissue, we model the stents as hollow solid stainless steel tubes. Modeling the mesh as a solid object reduces the computational complexity in HFSS. Chow et al. successfully used this same dipole and hollow solid stainless steel tube model at 2.4 GHz [23], [24]. Occhiuzzi et al. also used the hollow metal tube approximation in the 866–956 UHF RFID band [15]. The stent antenna dimensions are modeled according the previously stated length, width, wall thickness, and antenna gap feed.

While the same stent antenna is common to both *Model 1* and *Model 2* (i.e., only *Model 2* is experimentally verified with porcine tissue experiments), there are several key differences between the implants that interface to the stent antenna and the implant environment in both of these models. In *Model 1*, a 2 mm x 5 mm x 250 μm thick PCB with a biocompatible alumina coating interfaces to the stent antenna, via a 28 gauge wire antenna feed, to approximate any implanted electronics. A similar implant PCB size was used for evaluating wireless stent performance by Chow et al. [24]. Chow et al. used an alumina coating as a baseline biocompatible material in experiments for packaging the intraluminal implanted electronics [18]. In the *Model 1* environment, we model blood vessel tissue, blood, and plaque proliferation. The blood is modeled statically (i.e., not flowing); modeling flowing blood is beyond the scope of this work. We modeled the plaque as a hollow cylinder, as done by Occhiuzzi et al. [13], [15], at a 5 cm Type A lesion [44]. Plaque proliferation is modeled in three possible cases 0%, 50%, and 100% (See Supplementary Materials Section I-2 for further descriptions of the plaque, lesion types, and vasculature). At 0%, the stent only makes contact with blood vessel on its outside and blood on its inside. However, as plaque proliferates, both blood and plaque contact the stent and are present inside the stent. In *Model 2* (i.e., and the porcine tissue experiments), an 8.5 mm x 30 mm x 1.57 mm PCB containing the electronics described in Section II-F1 interfaces to the stent antenna via an SMA antenna feed (i.e., an SMA connector on the PCB mates with an SMA connector soldered to the stent antenna). Neither *Model 2* nor the porcine tissue experiments incorporate blood vessel, blood, and plaque. In lieu of blood, paper (i.e., $\epsilon_r = 3.2$ and loss tangent = 0.077 from Yang et al. [45]) was rolled and inserted inside the stents' inner diameter for structural support.

E. Experimental Porcine Tissue Model & Measurements

The dielectric properties of porcine tissue make them a good human tissue substitute [27]. The experimental porcine tissue model in this work was a picnic shoulder cut of meat from a large adult pig, which includes bone, muscle, fat, and skin. To the best of the authors' knowledge, few studies have reported data for *in vivo* and *ex vivo* porcine tissues (i.e., Hahn et al. [46], Peyman et al. [27], and Abdilla et al. [47]), and even fewer have reported data for pork muscle (i.e., Lyng et al. [48] and McCarthy et al. [49]). None of the previously reported data covers the frequency range used in this study. Therefore, we measured the dielectric properties of the porcine skin, fat, and muscle using the DAK-3.5 Dielectric Assessment Kit (Schmid & Partner Engineering AG, Zürich, Switzerland) from 200 – 1000 MHz. Bone was not measured, because of the need for good surface contact with the dielectric probe's planar interface. We compare our measurements with data from Peyman et al. and McCarthy et al., because their published data can be readily compared to our measured bandwidth. Pork muscle conductivity was extracted from McCarthy et al.'s data for dielectric loss, ϵ'' , using $\sigma = \omega\epsilon''\epsilon_0$, where ϵ_0 is the permittivity of free space. It is unclear whether Abdilla et al.'s data corresponds to either bovine or porcine tissue or a

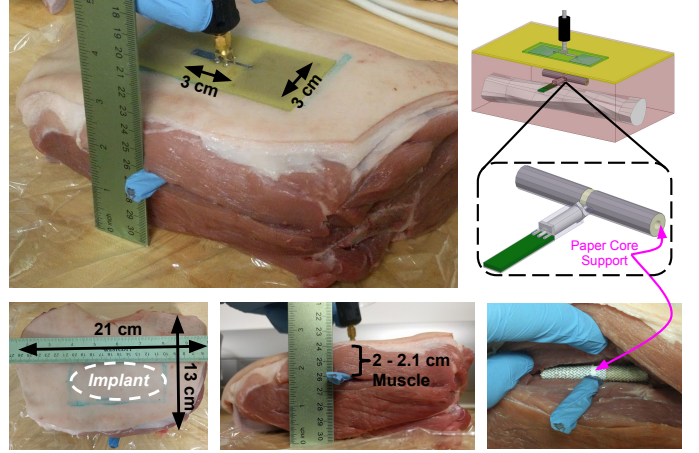


Fig. 2. Porcine tissue and *Model 2* simulation model. The implant is beneath approximately 0.2 cm of skin, 0.1 cm of fat, and 2.1 cm of muscle tissue. The electronics were covered by part of a blue nitrile glove for moisture protection.

combination of the two, and Hahn et al. only report data up to 100 MHz, which is below the measurement capability of the DAK-3.5 system. Lyng et al. investigated meats at three bands, 27.12 MHz, 915 MHz, and 2450 MHz, but their study largely focused on the 27.12 MHz and 2450 MHz bands, preventing comparison with our experiments.

The stent antenna and electronics were inserted into a pocket cut into the muscle. Figure 2 shows the approximate model dimensions and location of the implant. The implant was located beneath approximately 0.2 cm of skin, 0.1 cm of fat, and 2.1 cm of muscle tissue.

Six touch probe antennas were fabricated, with each of the antennas having a probe separation equal to its electrode width (e.g., 3 cm electrode width and 3 cm electrode separation). The touch probe was driven by the external driver electronics through a coaxial cable, discussed in the following sections. The skin was lightly abraded with fine-grain sandpaper to improve antenna-skin contact, as recommended by Hackworth [50]. Light pressure was applied to ensure total contact between the electrodes and the skin. The drive power was initially set arbitrarily high and then the touch probe antenna was swept along the porcine skin surface until the communication with the implant is achieved. With the implant found, the drive power was set below the implant's turn-on power threshold and then incrementally increased until implant communication resumes. The point at which communication resumes is the turn-on power threshold. Noting the turn-on power threshold and the touch probe drive power, G_A was determined. Three porcine tissue models were measured on three separate days.

F. Electronics

1) *Implanted and External Electronics*: The system's electronics include the external touch probe driver, the external demodulator, and an implanted power-to-frequency converter with a load modulator. The modulator alters the impedance seen at the implanted antenna terminals, as seen from the external electronics, at a rate proportional to the received

wireless power. The reason for measuring received power with the implant, rather than using cables for a two-port measurement on a vector network analyzer (VNA), as done by Keikhosravy et al. [25], is explained by Ho et al., who states that the conductive probes near the device disturb the surrounding fields in the tissue at the implant [26]. This fact is corroborated by Chow et al., who powered an implanted stent and its electronics from an external power source via wires, noting that the wire placement and orientation showed simulated gain variations from -3.6 to +2.3 dB [24].

This work presents an alternative to the work by Ho et al., who inserted a fiber optic cable into the tissue to observe an implant with a flashing LED whose pulse rate is proportional to the received power, by eliminating the need for a fiber optic cable or any other conduit to read the implant – reading the power level is done through the touch probe interface. For live animal or human measurements, the LED and fiber optical guide approach would be impractical, requiring both a percutaneous fiber wire and permanent vascular access, which carries major complications such as increased thrombosis, propagating the thrombosis downstream, and distal embolism [51], thereby leading to the same problem the stenting was set to treat.

The size of the implanted electronics in this work are also expected to disturb the fields at the implant; however, all the implanted circuitry is readily amenable to a monolithic implementation. The following sections describe electronics operating in the 315 MHz Industrial, Scientific and Medical (ISM) band. This ISM band is conveniently close to 308 MHz, which is the frequency corresponding to a 120 mm wavelength in muscle tissue (i.e., for the 60 mm half-wave stent dipole). A schematic of the implanted electronics is shown in Figure 3(a) and a schematic of the external electronics in Figure 3(b). Detailed descriptions of their designs and their benchmarking can be found in the Supplementary Materials.

2) *Full System Simulation* : A full system simulation is performed in LTSpice. The full system simulation model includes the external driver, the external demodulator, the implanted electronics, and a lumped element equivalent of the tissue – the T equivalent reciprocal two-port network [40]. The T equivalent model was previously used by Mandal and Sarpeshkar [52] and O’Driscoll [53] to model the transcutaneous wireless link between an external and implanted antenna. The T equivalent model, shown in Figure 4 is derived from the S-parameters described in Section II-C. The S-parameters are converted to impedance parameters (i.e., Z-parameters) using Eq. (6):

$$\mathbf{Z} = \begin{bmatrix} Z_{11} & Z_{12} \\ Z_{21} & Z_{22} \end{bmatrix} = \sqrt{\mathbf{Z}_0}(\mathbf{I} - \mathbf{S})^{-1}(\mathbf{I} + \mathbf{S})\sqrt{\mathbf{Z}_0} \quad (6)$$

where \mathbf{Z} is the Z-parameter matrix, \mathbf{S} is the two-port S-parameter matrix, \mathbf{I} is the identity matrix, and $\sqrt{\mathbf{Z}_0}$ is a diagonal matrix with its diagonal elements equal to the square-root of the system characteristic impedance, Z_0 . The Z-parameters are then used to calculate the impedance values of the series and shunt legs in the T equivalent model in Figure 4.

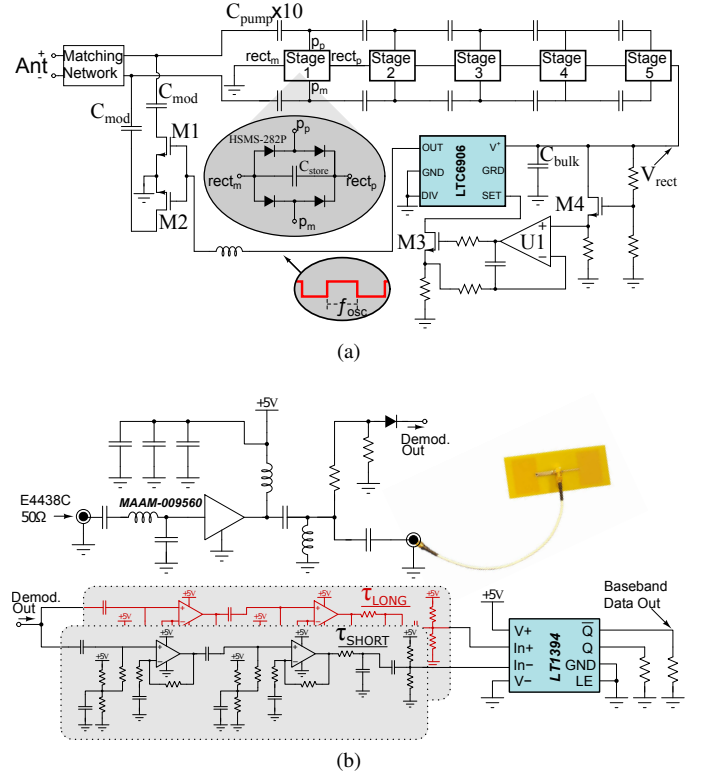


Fig. 3. (a) Implanted electronics schematic. (b) Touch probe driver and demodulator schematic.

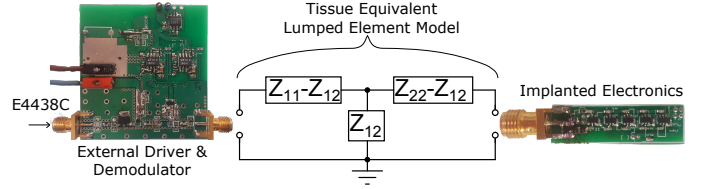


Fig. 4. Usage of the T equivalent model in terms of Z-parameters.

The full system simulation is performed for *Model 2* and compared to the experiments using the porcine tissue model in Figure 2. With the external driver side of the T equivalent model loaded by the external electronics, the output impedance at the implant-side of the T equivalent model is found by inserting the Z-parameters of Eq. (6) into Eq. (7):

$$Z_{out} = Z_{22} - \frac{Z_{12}Z_{21}}{Z_{11} + Z_S} \quad (7)$$

where $Z_S = 37.4 - j3.79$ and is the impedance looking into the driver electronics, and is the parallel combination of the impedance matched PA and the demodulator circuitry. Z_S could not easily be measured with the PA operating (i.e., a “hot- S_{22} ” measurement), so it is found by simulation in Designer using industry-supplied component models of the external electronics and an HFSS coaxial cable model. The implanted electronics are impedance matched to Z_{out} .

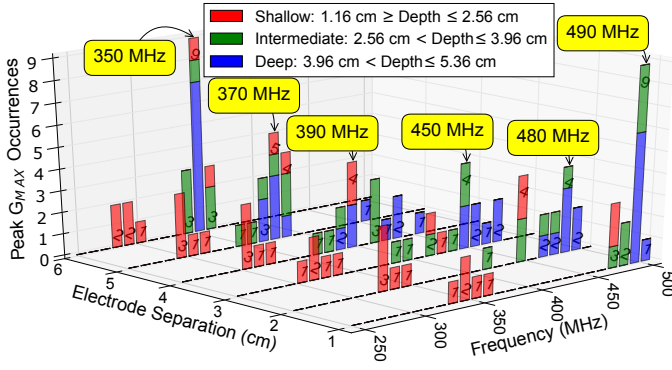


Fig. 5. Histogram showing peak G_{MAX} frequency occurrences for all tissue variations at each electrode separation in *Model 1* using 50% occlusion. Implant depth shown in three discrete groupings: shallow, intermediate, and deep.

III. RESULTS

A. Human Model Simulations

Figure 5 shows a histogram, for *Model 1* at 50% occlusion, of the frequency at which the G_{MAX} occurred for a given tissue variation at each electrode separation. The histogram also shows how many occurrences in each bin correspond to one of three tissue depths: shallow, intermediate, and deep. Note that from about 1 – 4 cm electrode separations, the intermediate and deep implant depths, the 433 MHz ISM band is the nearest operational band. Meanwhile, the majority of shallow depth implants are covered by the 315 MHz ISM band. These results indicate that the 308 MHz excitation far-field approximation for half-wave dipole operation in muscle tissue, discussed in Section II-C, was reasonable, but fails for increased implant depths.

At a 2.36 cm implant depth in Figure 5, from smallest to largest separation, the peak G_{MAX} frequencies are: 335, 320, 305, 300, 290, 285 MHz. This indicates that conducting the *Model 2* porcine tissue experiments at 315 MHz is likely a worthwhile operational frequency. Additionally, the histogram uncovers a trend that using a larger electrode separation results in a tighter distribution of peak G_{MAX} frequencies. For example, at a 6 cm electrode separation, the shallow, intermediate, and deep implant depths all share 315 MHz as the nearest operational frequency.

Figure 6 shows G_{MAX} for variations in fat thickness and vessel location for each electrode separation variation at 315 MHz. As electrode separation increases, performance at shallower depths improves only slightly, while at deeper implant depths, the performance improves substantially more. For example, at a 0.1 cm fat thickness, and vessel location of 0.87 cm, and a 1 cm electrode separation, $G_{MAX} = -12.6$ dB and an electrode separation of 6 cm, $G_{MAX} = -14.7$ dB. Meanwhile, at a 3.1 cm fat thickness, and vessel location of 2.07 cm, and an electrode separation of 1 cm, $G_{MAX} = -27.5$ dB and an electrode separation of 6 cm, $G_{MAX} = -23.2$ dB. Noting the fixed 3 cm electrode width in *Model 1*, the expectation that equal electrode separation and width maximizes gain, from Liu et al. [34], only holds true for the shallowest fat thickness, 0.1 cm. Even though performance improves with increasing

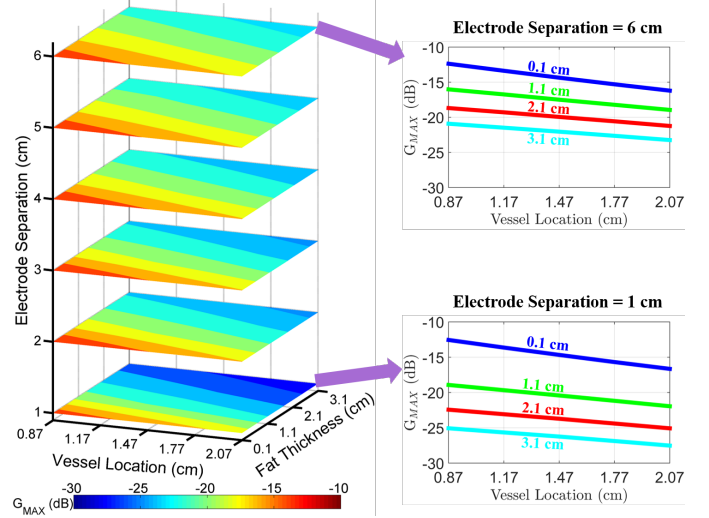


Fig. 6. G_{MAX} at 315 MHz for variations of fat thickness, vessel location, and electrode separation in *Model 1* at a 50% occlusion.

electrode separation, the improvement diminishes past about a 5 cm electrode separation, a trend supported by Hackworth's work conducted at lower frequencies [50].

From the figure, clearly vessel location and fat thickness affect the link gain differently. For a given electrode separation, variations in vessel location show a nearly constant change in link gain. Whereas, link gain sensitivity to variations in fat thickness can be greatly improved by selecting a larger electrode separation. For example, the difference in maximum available gain between 0.1 cm and 3.1 cm at a vessel location of 1.17 cm for an electrode separation of 1 cm is 12.0 dB and for a separation of 6 cm it is 8.11 dB. At a 1 cm electrode separation and a 1.17 cm vessel location, increasing fat thickness from 0.1 cm to 1.1 cm, 1.1 cm to 2.1 cm, and 2.1 cm to 3.1 cm, corresponds to a change in G_{MAX} of 6.04 dB, 3.40 dB, and 2.58 dB, respectively. Meanwhile, for a 6 cm electrode separation using the same fat thicknesses and vessel location, the change in G_{MAX} is 3.37 dB, 2.55 dB, and 2.20 dB, respectively.

Plaque proliferation showed a nearly constant affect for *Model 1*'s simulated model variations. Using 0% occlusion as the reference, for all tissue variations and electrode separation variations, G_{MAX} improved by 0.885 ± 0.0612 dB at 50% occlusion and improved by 0.966 ± 0.0180 dB at 100% occlusion. This result is supported by Occhiuzzi et al., who found that the turn-on power of an RFID tag reduced by about 3 dB across the entire ultra-high frequency (UHF) RFID band, when the disease progressed from a healthy vessel to 100% occlusion [15]. The 2 dB difference between our findings and Occhiuzzi et al.'s may be due our modeling of plaque as fat tissue, while Occhiuzzi et al. built liquid tissue phantoms with engineered dielectric properties using salt, sugar, and water.

Figure 7 shows the 10-gram peak spatial-average SAR values, extracted from HFSS/Designer, on the skin surface, for *Model 1* with 0% and 100% occlusions at a shallow (i.e., 0.1 cm fat, 0.87 cm vessel location), as well as at a deep implant depth (i.e., 2.1 cm fat, 2.07 cm vessel location),

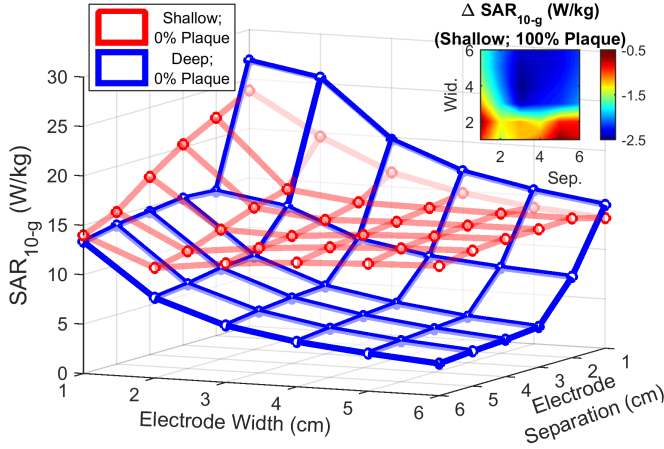


Fig. 7. SAR_{10-g} for *Model 1*.

but for 0% occlusion, only. For most electrode variations, shallower implant depths result in a higher SAR. At 0% occlusion for shallow implant depths and small electrode widths and separations, increasing electrode width reduces SAR only slightly more than increasing separation. Touch probes larger than about a 3 cm electrode width and separation show no further SAR improvement with increasing size; larger touch probes at a shallow depth even begin to increase SAR slightly. At 100% occlusion for a shallow implant depth, SAR improves across all electrode separation and width variations. Noting that the 0% occlusion for shallow implant depth begins to increase SAR slightly for larger touch probes, the 100% occlusion shows the opposite trend (i.e., decreases SAR).

The deep implant case uncovers a significant SAR improvement, compared to the shallow implant case, as touch probe size increases. In this case, increasing electrode separation reduces SAR the most, and diminishing SAR improvements begin at about a 3 cm electrode width and separation. Very small electrode separations present a major problem at deep implant depths, and show significantly poorer SAR performance across all electrode width variations compared to the shallow implant depth. These results indicate that the worst SAR performance will occur after initial stent deployment, and that small touch probes should be avoided, particularly for deep implants. Additionally, noting that the 10-gram peak spatial-average SAR limit is 2 W/kg, none of the antenna configurations can be used continuously without some duty cycling or drive power reduction; the latter limiting the available power for the implanted electronics.

Using *Model 1* with 0% occlusion for a deep implant depth (i.e., 2.1 cm fat, 2.07 cm vessel location), Table II shows the maximum available gain and 10-gram peak spatial-average SAR (i.e., from Figure 7) as well as the adjusted gain for $\%T_{on} = 100$ and $\%T_{on} = 20$. A 100% on-time corresponds to truly continuous monitoring, where no duty cycling is used. From the table, operating the system with antennas at $\%T_{on} = 100$ would necessitate reducing the 1 Watt drive power in order to meet SAR limits. Despite larger touch probes typically reducing SAR and improving power gain, it is undesirable to use too large an antenna, which may

TABLE II
 G_{MAX} AND SAR_{10-g} FOR EQUAL VALUES OF ELECTRODE SEPARATION AND WIDTH FOR *Model 1* WITH 0% OCCLUSION AT A DEEP IMPLANT DEPTH, 2.1 CM FAT AND 2.07 CM VESSEL LOCATION IMPLANT DEPTH. $G_{adj, SAR}$ SHOWN FOR $\%T_{on}$ VARIATIONS, AND TOUCH PROBES MEETING SAR REGULATIONS FOR A 1 WATT DRIVE ARE SHOWN HIGHLIGHTED.

(Sep., Wid.) (cm, cm)	G_{MAX} (dB)	SAR_{10-g} (W/kg)	$G_{adj, SAR}$ $\%T_{on} = 100$ (dB)	$G_{adj, SAR}$ $\%T_{on} = 20$ (dB)
(1, 1)	-27.5	26.9	-11.3	-4.29
(2, 2)	-25.0	13.5	-8.28	-1.29
(3, 3)	-23.4	6.82	-5.33	+1.66
(4, 4)	-22.4	5.25	-4.19	+2.80
(5, 5)	-21.9	4.10	-3.12	+3.87
(6, 6)	-21.6	3.24	-2.10	+4.89

TABLE III
LOADED NETWORK Z_{out} FOR THREE MODEL TYPES.

	<i>Model 1</i>	<i>Model 1</i> (varied Sep. and Width)	<i>Model 2</i> (varied Sep. and Width)
$\Re(Z_{out}) \Omega$	14.1 ± 1.57	13.0 ± 1.60	12.2 ± 0.0802
$\Im(Z_{out}) \Omega$	$j4.30 \pm 0.674$	$j4.23 \pm 0.759$	$j15.0 \pm 0.107$

not make full skin-contact due to the curvature of the human leg. Thus, using the smallest antenna capable of meeting a desired available power for implanted electronics is preferred. The antenna with electrode width and separation both equal to 3 cm at $\%T_{on} = 20$ is the smallest antenna capable of adhering to SAR regulations. For this touch probe, the drive power can even be increased by 1.66 dB, while still meeting regulatory limits.

The output impedance, Z_{out} from Eq. (7), of both *Model 1* and *Model 2* showed little variation across tissue and antenna dimension variations. This simplifies the impedance matching network for the implanted electronics. Table III shows Z_{out} for *Model 1*, *Model 1* where the electrode separation and width were varied in SAR simulations, and *Model 2*. The slightly larger Z_{out} inductance observed in *Model 2* is likely due to the large implanted electronics and SMA connectors, which do not appear in *Model 1*.

B. Porcine Model Simulations and Experiments

The measured dielectric properties for skin, fat, and muscle are shown in Figure 8, along with extracted data points from literature for comparison. Data for 250 kg adult pigs from Peyman et al. were used [27], because our porcine tissue was harvested from large adult pigs. Upon dissection of the fat layer, an abundance of superficial fascia, which is primarily composed of collagen, was found. No published data could be found for porcine superficial fascia. However, Peyman et al. report data for cartilage, which contains collagen. Thus, we compare the measured data for fascia with Peyman et al.'s data for cartilage, which was only reported for 50 kg pigs. The muscle and skin measurements agree well with those from literature. Cartilage's measured data and data from literature show some disagreement, but this is likely due to Peyman et al.'s lack of cartilage data for 250 kg pigs; 14 of the 16 tissues reported by Peyman et al. show a decreasing dielectric

TABLE IV
USING *Model 2*, SHOWING G_A AND T EQUIVALENT MODEL PARAMETERS FOR EQUAL VALUES OF ELECTRODE SEPARATION AND WIDTH.

(Sep., Wid.) (cm, cm)	G_A (dB)	$Z_{11} - Z_{12}$	Z_{12}	$Z_{22} - Z_{12}$
(1, 1)	-18.5	$28.4 - j2.15$	$0.651 + j4.48$	$11.4 + j10.7$
(2, 2)	-17.9	$27.3 + j15.6$	$0.816 + j4.89$	$11.1 + j10.3$
(3, 3)	-18.2	$28.7 + j30.7$	$0.800 + j5.13$	$11.1 + j10.1$
(4, 4)	-19.0	$31.4 + j45.1$	$0.664 + j5.29$	$11.2 + j9.93$
(5, 5)	-19.9	$35.2 + j59.3$	$0.468 + j5.43$	$11.4 + j9.83$
(6, 6)	-20.8	$40.2 + j73.3$	$0.235 + j5.58$	$11.7 + j9.67$

property trend as the pig size increases, and it is likely that cartilage from a 250 kg pig would also show this trend and improve the agreement between the data. The two tissues that do not show a decreasing trend are intervertebral disc centre and tongue. Tongue shows relatively constant properties across pig weight. The intervertebral disc centre, which contains collagen, does decrease from small to large pigs, but shows a slight increase from small to medium pigs. Because the intervertebral disc centre contains collagen, along with noting the decreasing dielectric property trend for most tissues, we can also reasonably expect cartilage from a 250 kg pig to be closer to our measured data.

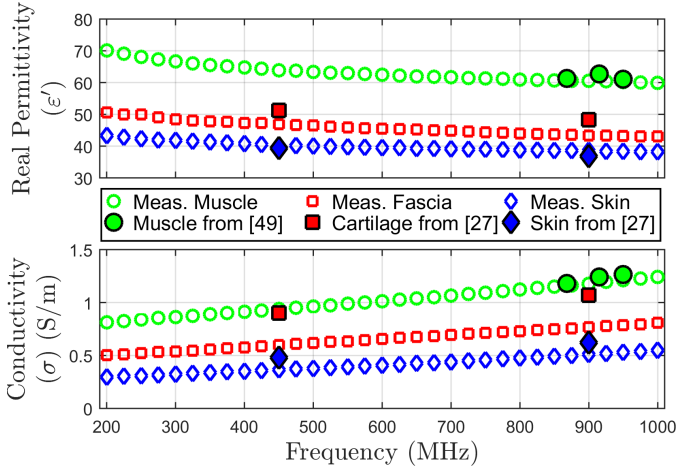


Fig. 8. Measured dielectric properties of porcine skin, fat (i.e., mostly superficial fascia), and muscle along with data found in literature.

Table IV shows the simulated expected available gain, G_A , for *Model 2* along with the T model equivalent parameters for building the lumped element models used in the full system simulation. The simulated *Model 2* implant depth is at 0.19 cm skin, 0.1 cm fat, and 2.07 cm muscle, the same used as a variation in *Model 1*, but with the measured dielectric properties. Note in Table IV that the bottom two touch probe sizes (i.e., both electrode width and separation each equal to 5 cm and 6 cm) could not be measured with the porcine experiments (see Figure 9), and thus, were not simulated.

Figure 9 shows the simulated available gain for *Model 2* from HFSS/Designer, the full system simulation in LTSpice using T model equivalent parameters, and the measured avail-

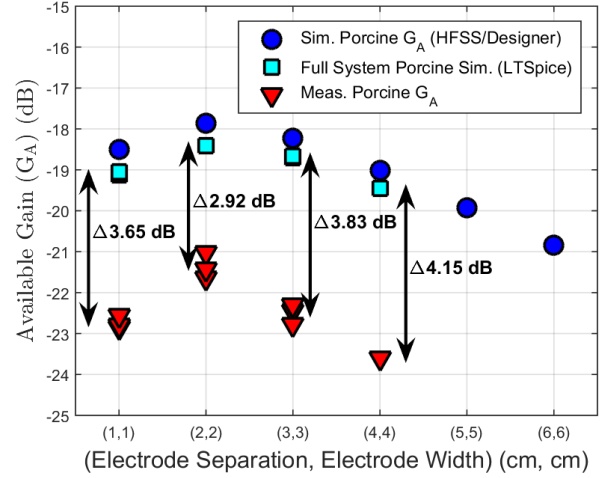


Fig. 9. G_A for *Model 2* simulations and porcine tissue experiments using various touch probes. Implant depth is detailed in Figure 2. Arrows indicate the mean difference between full system simulated and measured data at each antenna size.

able gain using the porcine tissue. Both the HFSS/Designer and LTSpice simulations in the figure use the dielectric properties from the measured porcine tissue in Figure 8. G_A is computed by taking the difference, in decibels, between turn-on power threshold for the impedance matched case in Figure 5 in the Supplementary Material and the available power from the external driver, $P_{out,PA}$, (i.e., from VSG drive power where the implant turn-on threshold occurs) in Figure 6 in the Supplementary Material.

It should be noted that there were several limitations in the porcine model data collection. For antennas with both an electrode width and separation equal to 5 cm and 6 cm, measurements could not be obtained because of the PA output compression limiting the maximum available output power from the external driver, at about 24.67 dBm in Figure 6 found in the Supplementary Material. This is also the cause of obtaining only a single measurement (i.e., and a single full system simulation data point) for the (4,4) touch probe across the three porcine model experiments.

The full system simulation in LTSpice shows good agreement with the available gain calculated from HFSS/Designer. In the measured data, three measurements were obtained for (1,1), (2,2), and (3,3). Only one measurement could be obtained for (4,4). Three unique drive powers were needed for (1,1), two for (3,3) and one for (2,2) and (4,4). The full system simulation was performed for each unique drive power variation. The largest difference between the full system simulation and the simulated available gains is -0.618 dB and occurs at (1,1); the mean difference across all four simulated touch probe dimensions is -0.522 ± 0.0713 dB. The mean and standard deviation of the measured available gain data at each antenna size were: -22.7 ± 0.154 dB for (1,1), -21.4 ± 0.314 dB for (2,2), and -22.5 ± 0.244 dB (3,3); (4,4) had only one data at -23.6 dB. The mean difference between the full system simulation data and the measured data are, 3.65 dB [min: 3.80, max: 3.44], 2.92 dB [min: 3.23, max: 2.61], 3.83 dB

[min: 4.07, max: 3.63], and 4.15 dB, for increasing antenna width and separation, respectively. The differences between measurement and simulation results can be attributed to several reasons, including the curvature of the porcine tissue model, which was not modeled, the quality of the electrode-skin contact (i.e., due to skin layers that raise contact impedance), which Hackworth noted greatly affect system performance [50], and simplification of the stent wire mesh with a solid stainless steel tube.

IV. DISCUSSION

Current PAD monitoring protocols determine the degree of restenosis every 3 to 6 months, provided the patient complies with hospital visits. Current Doppler Duplex imaging machines for screening stenoses are impractical for rapid detection. More frequent monitoring, possibly every month or every week, is desirable. Discovering a stenosis 3 or 6 months after it has begun means the disease may have already progressed to an advanced state or an occlusion. For the deep implant case in Fig. 7, every antenna in Table II adheres to the SAR limits for a one minute reading each month or week, thereby eliminating the need for large touch probes to improve gain and SAR and reducing the chance for poor skin contact. An additional implication of this monitoring protocol is that significantly deeper implants can be powered due to the increased touch probe drive power.

The familiar output of the Doppler Duplex imaging machine, a Doppler sonogram, has yet to be reported in literature for wireless implanted restenosis monitors. This imaging tool offers a real-time continuous view of restenosis degree. A wireless stent monitor that competes with Doppler Duplex imagers would also need to provide a real-time continuous intraluminal velocity/flow readings. Both SAR regulatory limits and the transduced Doppler spectrum are a barrier to truly continuous operation, and consequently, they set bounds on the implant powered-on time, $\%T_{on}$. In order to reach deep implants, the powered-on time should be minimized during the SAR averaging period. However, conversely, the powered-on time needs to be sufficiently long for capturing multiple cycles of the Doppler blood flow signals. We derive an appropriate $\%T_{on}$ by examining the power consumption of reported wireless implanted blood flow monitors followed by the expected Doppler spectrum in a diseased vessel.

Wireless implanted blood flow monitors have found use in animal studies [54], in artificial grafts [55], [56], and free flap studies [57]. DiPietro and Meindl reported a device that consumed 10 mW, the smallest found through literature [54]. Despite the trend for integrated circuit technology improvements leading to lower power consumption, the ultrasonic piezoelectric transducers for blood flow monitoring typically require appreciable amounts of power. Current state-of-the-art transducers for measuring blood flow can do so with a 500 μ W drive, according to Vilkomerson and Chilipka [55]. A simulation using the same 5-stage Cockcroft-Walton rectifier in this work for a 10.5 mW load (i.e., assuming a 3 V load voltage) with an unmatched 50 Ω drive source impedance showed a 50 μ s start-up time. As plaque proliferation increases, the peak

velocity increases as much as 100% along with significant spectral broadening according to Guo et al. [22]. However, the wall filter, often used in Doppler systems to filter slow-moving tissue or vessel wall noise, sets the lower bound of the Doppler bandwidth. Holland et al. used 50 Hz, while Guo et al. used 100 Hz. Ten cycles at 50 Hz plus the rectifier start-up time results in a required 200.05 ms power-on time for a single reading. For real-time operation, one reading is required each second: approximately $T_{on} = 0.20$ (exactly: $T_{on} = 0.20005$). Any touch probe antenna with a SAR rating less than 10 W/kg operating at $T_{on} = 0.20$ will satisfy the real-time continuous monitoring need for wireless implanted restenosis monitors to compete with Doppler Duplex imaging machines.

The simulation and experimental measurement agreement in this work represent the best accuracy reported for wireless stent monitoring systems – comparing the simulation-to-measurement disagreement max/min bounds of 2.61 – 4.15 dB in this work to that from Chow et al. of 3.5 – 6.6 dB [24]. Improvements were accomplished through a combination of co-simulation of both the tissue models and circuitry and the dielectric properties of tissues, which were not previously considered by Chow et al [24]. Simulation accuracy using both proprietary (ANSYS Designer/HFSS) and free (LTSpice) software were nearly the same. The high simulation accuracy improves confidence in future PAD monitor development.

In this work, we measured the dielectric properties of our experimental tissue model. We unexpectedly found fat tissue with a high concentration of superficial fascia, which has wildly different dielectric properties than fat. Simulation models developed by Chow et al. used human tissue dielectrics from Gabriel et al. [35]), and did not consider the dielectric differences between humans and the 35 – 40 kg pigs used in their experiments. The dielectric properties of porcine tissues change based on the animal’s age and weight. With increasing age and weight, most swine tissues’ permittivity and conductivity decrease, primarily due to a reduction in water content, according to Peyman et al. [27]. Peyman et al.’s work relates 10 kg pigs to human children aged 1–4 years, 50 kg pigs to humans aged 11–13 years, and 250 kg pigs to human adults. Atherosclerosis predominantly affects adults [58], therefore using properties from larger pigs could improve the simulation-measurement differences in Chow et al.’s study. For example, previously considered values for fat tissue at 2400 MHz in Chow et al.’s and Gabriel et al.’s [35] works show that the conductivity (i.e., the loss mechanism) of 50 kg pigs is approximately a factor of 3 greater than that for humans, while for 250 kg pigs, only a factor of 1.3 greater. Consequently, more loss is expected in measurements with a 50 kg pig compared to a human, which is corroborated by Chow et al.’s study – the 35–40 pig measurements overestimated the loss compared to that for human dielectric simulations.

The implications of these dielectric property differences uncover an important requirement for future wireless stent monitoring systems: animal studies must use an animal model indicative of the population affected by atherosclerosis. Selecting a large adult pig for future studies has a two-fold benefit. First, the transcutaneous wireless link is expected to more closely match that in humans. Second, investigating a

wireless re-stenosis monitor, outfitted with Doppler sensors for displaying a Doppler sonogram, will also need an appropriate animal model whose acoustic blood properties match closely to that of humans. The primary source of acoustic scattering (i.e., the reflected signal from which the Doppler signal is extracted) in blood are erythrocytes – red blood cells (RBCs). Both RBC size and aggregation have a significant impact on the acoustic scattering. The RBC size in pigs are comparable to those of humans [59]. The RBC aggregability in swine blood is similar to human blood [60], and better represents this effect than other animal models [61]. The strong relationship between RBC aggregation and turbulent flow [62], which increases significantly with increasing stenosis degree [22], indicates that porcine animal models are the most appropriate species for this type of study.

It should be noted that there are several limitations of this work. Blood vessel, blood, and plaque were not modeled in *Model 2* nor experimentally simulated in the porcine tissue experiments. It is unknown whether or not hemodynamics in the leg vessels would affect the the wireless power gain and SAR performance of the monitoring system. Future experiments could investigate this problem by using a syringe pump, such as the NE-1000 (New Era Pump Systems, Inc., Farmingdale, NY, USA) used in our previous work with porcine blood flow monitoring [57], to pump blood in a tube through the stent's center in lieu of the paper structural support used in this research. With this blood pump in place, vessel and plaque can be experimentally simulated by harvesting blood vessel and fat (i.e., plaque can be modeled as fat [14]) from porcine tissue and wrapping them around the tube carrying blood. By incorporating these tissues and blood, a more comprehensive and accurate *ex vivo* model could be developed.

From a clinical perspective, there are a number of potential practical barriers and limitations to using a stent antenna monitoring system. For example, manufacturing the stent antenna, with its two stent dipole arms and biocompatibly packaged electronics suspended between the two arms, will likely require additional structural support and modification to the stents themselves. As far as types of stents to be used in stent monitoring systems, Chow et al. noted that the self-expandable stents, which were used in our research, are more desirable from a surgical perspective (e.g., better shape and structural deformation properties) than balloon-expandable stents [24]. The self-expandable stents are also more desirable from an electrical perspective, because balloon expansion requires high pressures that could damage electronics located near or inside the stent. Therefore, any additional structural modifications to create the stent antenna must minimally impact the benefits of using self-expandable stents. With regard to the safety of deploying and using the stent monitoring system, both SAR effects and biocompatibility can affect adoption of this technology. While exposure to electromagnetic non-ionizing radiation has not been linked to an increased mortality rate [43], [63], the links between complications after stent placement (i.e., thrombosis and restenosis) and mortality are evident [64], [65] and likely to pose a more immediate threat to patient safety. With regard to biocompatibility, thrombosis and an inflammatory response is an expected to occur simply

because a foreign object is in the body. Chow et al. evaluated biocompatible packaging materials for their inflammation and fibrous encapsulation responses for use in their stent energy harvesting cardiovascular pressure monitor [18]. Their *in vivo* studies found the liquid crystal polymer (LCP) material performed the best of the tested materials and resulted in no inflammation at the end of their four-week long study. To supplement efforts to reduce restenosis, thrombosis, and inflammation in the stent antenna implant, it is possible that drug-eluting stents (DES) can offer an advantage over simple bare-metal stents (BMS) [66]. However, it is still unclear whether DES are an improvement over BMS when used to treat PAD [67].

This paper shows how to safely and wirelessly power a PAD restenosis monitor. We validated simulation models with *ex vivo* porcine measurements using an implanted wireless power-to-frequency converter and touch probe antenna reader system. Our results demonstrated the most accurate simulation-to-measurement agreement found in literature, and they provide recommendations for touch probe interfaces needed to meet safety regulations and desired power delivery to an implant. The proposed system can be used to develop at-home wireless implanted restenosis monitors that use the familiar Doppler technique, in order to compete with expensive Doppler Duplex imaging machines used in hospitals.

V. CONCLUSION

This paper shows how to safely and wirelessly power a PAD restenosis monitor. We validated simulation models with *ex vivo* porcine measurements using an implanted wireless power-to-frequency converter and touch probe antenna reader system. Our results demonstrated the most accurate simulation-to-measurement agreement found in literature, and they provide recommendations for touch probe interfaces needed to meet safety regulations and desired power delivery to an implant. For general PAD monitoring, the 3 cm x 3 cm square electrode touch probe is a good candidate due to its SAR performance, power gain, and small size, which improves skin contact on the human body's contours. The proposed system can be used to develop at-home wireless implanted restenosis monitors that use the familiar Doppler technique, in order to compete with expensive Doppler Duplex imaging machines used in hospitals.

ACKNOWLEDGMENTS

The study was supported by the Center for Medical Innovation under award number F 064-2013.

REFERENCES

- [1] R. Ross, "The pathogenesis of atherosclerosis: a perspective for the 1990s," *Nature*, vol. 362, no. 6423, pp. 801–809, 1993.
- [2] M. Lovell, K. Harris, T. Forbes, G. Twillman, B. Abramson, M. H. Criqui, P. Schroeder, E. R. Mohler, A. T. Hirsch *et al.*, "Peripheral arterial disease: lack of awareness in Canada," *Canadian Journal of Cardiology*, vol. 25, no. 1, pp. 39–45, 2009.
- [3] R. C. Pasternak, M. H. Criqui, E. J. Benjamin, F. G. R. Fowkes, E. M. Isselbacher, P. A. McCullough, P. A. Wolf, and Z.-J. Zheng, "Atherosclerotic vascular disease conference writing group I: epidemiology," *Circulation*, vol. 109, no. 21, pp. 2605–2612, 2004.

- [4] E. Selvin and T. P. Erlinger, "Prevalence of and risk factors for peripheral arterial disease in the United States results from the national health and nutrition examination survey, 1999–2000," *Circulation*, vol. 110, no. 6, pp. 738–743, 2004.
- [5] R. Ramos, M. Quesada, P. Solanas, I. Subirana, J. Sala, J. Vila, R. Masiá, C. Cerezo, R. Elosua, M. Grau *et al.*, "Prevalence of symptomatic and asymptomatic peripheral arterial disease and the value of the ankle-brachial index to stratify cardiovascular risk," *European Journal of Vascular and Endovascular Surgery*, vol. 38, no. 3, pp. 305–311, 2009.
- [6] J. Lammer, M. Bosiers, T. Zeller, M. Schillinger, E. Boone, M. J. Zaugg, P. Verta, L. Peng, X. Gao, and L. B. Schwartz, "First clinical trial of nitinol self-expanding everolimus-eluting stent implantation for peripheral arterial occlusive disease," *Journal of vascular surgery*, vol. 54, no. 2, pp. 394–401, 2011.
- [7] G. S. R. Muradin, J. L. Bosch, T. Stijnen, and M. G. M. Hunink, "Balloon dilation and stent implantation for treatment of femoropopliteal arterial disease: Meta-analysis," *Radiology*, vol. 221, no. 1, pp. 137–145, 2001.
- [8] J. Radermacher, A. Chavan, J. Bleck, A. Vitzthum, B. Stoess, M. J. Gebel, M. Galanski, K. M. Koch, and H. Haller, "Use of Doppler ultrasonography to predict the outcome of therapy for renal-artery stenosis," *New England Journal of Medicine*, vol. 344, no. 6, pp. 410–417, 2001.
- [9] M. M. McDermott, J. M. Guralnik, L. Ferrucci, L. Tian, K. Liu, Y. Liao, D. Green, R. Sufit, F. Hoff, T. Nishida *et al.*, "Asymptomatic peripheral arterial disease is associated with more adverse lower extremity characteristics than intermittent claudication," *Circulation*, vol. 117, no. 19, pp. 2484–2491, 2008.
- [10] E. Vermeire, H. Hearnshaw, P. Van Royen, and J. Denekens, "Patient adherence to treatment: three decades of research. a comprehensive review," *Journal of clinical pharmacy and therapeutics*, vol. 26, no. 5, pp. 331–342, 2001.
- [11] M. H. Wholey, N. Al-Mubarek, and M. H. Wholey, "Updated review of the global carotid artery stent registry," *Catheterization and cardiovascular interventions*, vol. 60, no. 2, pp. 259–266, 2003.
- [12] D. E. Cutlip, D. S. Baim, K. K. Ho, J. J. Popma, A. J. Lansky, D. J. Cohen, J. P. Carrozza, M. S. Chauhan, O. Rodriguez, and R. E. Kuntz, "Stent thrombosis in the modern era. A pooled analysis of multicenter coronary stent clinical trials," *Circulation*, vol. 103, no. 15, pp. 1967–1971, 2001.
- [13] C. Occhiuzzi, G. Contri, and G. Marrocco, "RFID STENTag for passive vascular monitoring," in *Proceedings of the 5th European Conference on Antennas and Propagation*. IEEE, 2011, pp. 3476–3478.
- [14] F. Daschner, S. Hoffmann, R. Knochel, M. Jerosch-Herold, and C. Rickers, "Resonant stents for non-invasive monitoring of restenosis," in *2011 41st European Microwave Conference*. IEEE, 2011, pp. 972–975.
- [15] C. Occhiuzzi, G. Contri, and G. Marrocco, "Design of implanted RFID tags for passive sensing of human body: the STENTag," *IEEE Transactions on Antennas and Propagation*, vol. 60, no. 7, pp. 3146–3154, 2012.
- [16] K. Takahata, A. DeHennis, K. D. Wise, and Y. B. Gianchandani, "Stentenna: a micromachined antenna stent for wireless monitoring of implantable microsensors," in *Proceedings of the 25th Annual International Conference of the IEEE Engineering in Medicine and Biology Society*, vol. 4. IEEE, 2003, pp. 3360–3363.
- [17] K. Takahata, Y. B. Gianchandani, and K. D. Wise, "Micromachined antenna stents and cuffs for monitoring intraluminal pressure and flow," *Journal of Microelectromechanical Systems*, vol. 15, no. 5, pp. 1289–1298, 2006.
- [18] E. Y. Chow, A. L. Chlebowski, S. Chakraborty, W. J. Chappell, and P. P. Irazoqui, "Fully wireless implantable cardiovascular pressure monitor integrated with a medical stent," *IEEE Transactions on Biomedical Engineering*, vol. 57, no. 6, pp. 1487–1496, 2010.
- [19] A. D. DeHennis and K. D. Wise, "A fully integrated multisite pressure sensor for wireless arterial flow characterization," *Journal of Microelectromechanical Systems*, vol. 15, no. 3, pp. 678–685, 2006.
- [20] K. Keikhosravy, P. Kamalinejad, L. Keikhosravy, A. Zargar-Yazd, K. Takahata, and S. Mirabbasi, "A fully integrated telemonitoring system for diagnosing in-stent restenosis," in *2014 IEEE Biomedical Circuits and Systems Conference*. IEEE, 2014, pp. 392–395.
- [21] F. G. R. Fowkes, D. Rudan, I. Rudan, V. Aboyans, J. O. Denenberg, M. M. McDermott, P. E. Norman, U. K. Sampson, L. J. Williams, G. A. Mensah *et al.*, "Comparison of global estimates of prevalence and risk factors for peripheral artery disease in 2000 and 2010: a systematic review and analysis," *The Lancet*, vol. 382, no. 9901, pp. 1329–1340, 2013.
- [22] Z. Guo, L.-G. Durand, L. Allard, G. Cloutier, and H. C. Lee, "Classification of lower limb arterial stenoses from doppler blood flow signal analysis with time-frequency representation and pattern recognition techniques," *Ultrasound in medicine & biology*, vol. 20, no. 4, pp. 335–346, 1994.
- [23] E. Y. Chow, B. Beier, Y. Ouyang, W. J. Chappell, and P. P. Irazoqui, "High frequency transcutaneous transmission using stents configured as a dipole radiator for cardiovascular implantable devices," in *2009 IEEE MTT-S International Microwave Symposium Digest*. IEEE, 2009, pp. 1317–1320.
- [24] E. Y. Chow, Y. Ouyang, B. Beier, W. J. Chappell, and P. P. Irazoqui, "Evaluation of cardiovascular stents as antennas for implantable wireless applications," *IEEE Transactions on Microwave Theory and Techniques*, vol. 57, no. 10, pp. 2523–2532, 2009.
- [25] K. Keikhosravy, A. Zargar-Yazd, and S. Mirabbasi, "On the use of smart stents for monitoring in-stent restenosis," in *2012 Annual International Conference of the IEEE Engineering in Medicine and Biology Society*. IEEE, 2012, pp. 3231–3234.
- [26] J. S. Ho, A. J. Yeh, E. Neofytou, S. Kim, Y. Tanabe, B. Patlolla, R. E. Beygui, and A. S. Poon, "Wireless power transfer to deep-tissue microimplants," *Proceedings of the National Academy of Sciences*, vol. 111, no. 22, pp. 7974–7979, 2014.
- [27] A. Peyman, C. Gabriel, E. Grant, G. Vermeeren, and L. Martens, "Variation of the dielectric properties of tissues with age: the effect on the values of sar in children when exposed to walkie-talkie devices," *Physics in medicine and biology*, vol. 54, no. 2, p. 227, 2008.
- [28] M. Maksimovic, "Whether obesity is associated with peripheral arterial disease," *Angiology: Open Access*, vol. 2, p. e104, 2013.
- [29] J. A. Beckman, M. A. Creager, and P. Libby, "Diabetes and atherosclerosis: epidemiology, pathophysiology, and management," *Journal of the American Medical Association*, vol. 287, no. 19, pp. 2570–2581, 2002.
- [30] H.-Y. Lin, M. Takahashi, K. Saito, and K. Ito, "Performance of implantable folded dipole antenna for in-body wireless communication," *IEEE Transactions on Antennas and Propagation*, vol. 61, no. 3, pp. 1363–1370, 2013.
- [31] H. Miao, S. M. Gracewski, and D. Dalecki, "Ultrasonic excitation of a bubble inside a deformable tube: Implications for ultrasonically induced hemorrhage," *The Journal of the Acoustical Society of America*, vol. 124, no. 4, pp. 2374–2384, 2008.
- [32] Y. Rahmat-Samii and J. Kim, "Implanted antennas in medical wireless communications," *Synthesis Lectures on Antennas*, vol. 1, no. 1, pp. 1–82, 2005.
- [33] X. Liu, J. R. Stachel, E. Stachel, M. H. Mickle, and J. L. Berger, "The UHF Gen 2 RFID system for transcatheter operation for orthopedic implants," in *2013 IEEE International Instrumentation and Measurement Technology Conference*. IEEE, 2013, pp. 1620–1623.
- [34] X. Liu, J. L. Berger, A. Ogirala, and M. H. Mickle, "A touch probe method of operating an implantable RFID tag for orthopedic implant identification," *IEEE Transactions on Biomedical Circuits and Systems*, vol. 7, no. 3, pp. 236–242, 2013.
- [35] D. Andreuccetti, R. Fossi, and C. Petrucci, "An internet resource for the calculation of the dielectric properties of body tissues in the frequency range 10 Hz–100 GHz. IFAC-CNR, Florence (Italy). Based on data published by C. Gabriel *et al.* in 1996. [Online]. Available: <http://niremf.ifac.cnr.it/tissprop/>
- [36] W. G. Scanlon and N. E. Evans, "Numerical analysis of bodyworn UHF antenna systems," *Electronics & Communication Engineering Journal*, vol. 13, no. 2, pp. 53–64, 2001.
- [37] J. Kim and Y. Rahmat-Samii, "Implanted antennas inside a human body: Simulations, designs, and characterizations," *IEEE Transactions on microwave theory and techniques*, vol. 52, no. 8, pp. 1934–1943, 2004.
- [38] E. Y. Chow, C.-L. Yang, A. Chlebowski, S. Moon, W. J. Chappell, and P. P. Irazoqui, "Implantable wireless telemetry boards for *in vivo* transocular transmission," *IEEE Transactions on Microwave Theory and Techniques*, vol. 56, no. 12, pp. 3200–3208, 2008.
- [39] C. L. Brace, "Microwave tissue ablation: biophysics, technology, and applications," *Critical Reviews™ in Biomedical Engineering*, vol. 38, no. 1, 2010.
- [40] D. M. Pozar, *Microwave Engineering*, 4th ed. Wiley, 2011, ch. Microwave Amplifier Design.
- [41] E. Moradi, S. Amendola, T. Björninen, L. Sydänheimo, J. M. Carmena, J. M. Rabaey, and L. Ukkonen, "Backscattering neural tags for wireless brain-machine interface systems," *IEEE Transactions on Antennas and Propagation*, vol. 63, no. 2, pp. 719–726, 2015.

- [42] "IEEE standard for safety levels with respect to human exposure to radio frequency electromagnetic fields, 3 kHz to 300 GHz," *IEEE Std C95.1-2005 (Revision of IEEE Std C95.1-1991)*, pp. 1–238, April 2006.
- [43] I. Guideline, "Guidelines for limiting exposure to time-varying electric, magnetic, and electromagnetic fields (up to 300 GHz)," *Health Phys.*, vol. 74, no. 4, pp. 494–522, 1998.
- [44] L. Norgren, W. R. Hiatt, J. A. Dormandy, M. R. Nehler, K. A. Harris, F. G. R. Fowkes, and Tasc II Working Group and others, "Inter-society consensus for the management of peripheral arterial disease (TASC II)," *European Journal of Vascular and Endovascular Surgery*, vol. 33, no. 1, pp. S1–S75, 2007.
- [45] L. Yang, A. Rida, R. Vyas, and M. M. Tentzeris, "RFID tag and RF structures on a paper substrate using inkjet-printing technology," *IEEE Transactions on Microwave Theory and Techniques*, vol. 55, no. 12, pp. 2894–2901, 2007.
- [46] G. M. Hahn, P. Kernahan, A. Martinez, D. Pounds, S. Prionas, T. Anderson, and G. Justice, "Some heat transfer problems associated with heating by ultrasound, microwaves, or radio frequency," *Annals of the New York Academy of Sciences*, vol. 335, no. 1, pp. 327–346, 1980.
- [47] L. Abdilla, C. Sammut, and L. Z. Mangion, "Dielectric properties of muscle and liver from 500 mhz–40 ghz," *Electromagnetic biology and medicine*, vol. 32, no. 2, pp. 244–252, 2013.
- [48] J. Lyng, L. Zhang, and N. Brunton, "A survey of the dielectric properties of meats and ingredients used in meat product manufacture," *Meat Science*, vol. 69, no. 4, pp. 589–602, 2005.
- [49] U. M. McCarthy, G. Ayalew, F. Butler, K. Mc Donnell, J. Lyng, and S. Ward, "Permittivity of meat fish and their components at uhf rfid frequencies and industry relevant temperatures," *Agricultural Engineering International: CIGR Journal*, 2009.
- [50] S. A. Hackworth, "Design, optimization, and implementation of a volume conduction energy transfer platform for implantable devices," Ph.D. dissertation, University of Pittsburgh, 2010.
- [51] R. C. Lam, S. Shah, P. L. Faries, J. F. McKinsey, K. C. Kent, and N. J. Morrissey, "Incidence and clinical significance of distal embolization during percutaneous interventions involving the superficial femoral artery," *Journal of vascular surgery*, vol. 46, no. 6, pp. 1155–1159, 2007.
- [52] S. Mandal and R. Sarpeshkar, "Power-efficient impedance-modulation wireless data links for biomedical implants," *IEEE Transactions on Biomedical Circuits and Systems*, vol. 2, no. 4, pp. 301–315, 2008.
- [53] S. O'Driscoll, "Adaptive signal acquisition and power delivery for implanted medical devices," Ph.D. dissertation, Stanford University, 2009.
- [54] D. M. Di Pietro and J. D. Meindl, "Optimal system design for an implantable CW Doppler ultrasonic flowmeter," *IEEE Transactions on Biomedical Engineering*, no. 3, pp. 255–264, 1978.
- [55] D. Vilkomerson and T. Chilipka, "Implantable Doppler system for self-monitoring vascular grafts," in *2004 IEEE Ultrasonics Symposium*, vol. 1. IEEE, 2004, pp. 461–465.
- [56] D. Vilkomerson, T. Chilipka, J. Bogan, J. Blebea, R. Choudry, J. Wang, M. Salvatore, V. Rotella, and K. Soundararajan, "Implantable ultrasound devices," in *Proceedings of SPIE, Medical Imaging, Ultrasonic Imaging, and Signal Processing*, vol. 6920, March 2008, pp. 69 200C–69 200C–11.
- [57] M. A. Rothfuss, N. G. Franconi, J. V. Unadkat, M. L. Gimbel, A. STAR, M. H. Mickle, and E. Sejdić, "A system for simple real-time anastomotic failure detection and wireless blood flow monitoring in the lower limbs," *IEEE Journal of Translational Engineering in Health and Medicine*, vol. 4, pp. 1–15, 2016.
- [58] A. S. Go, D. Mozaffarian, V. L. Roger, E. J. Benjamin, J. D. Berry, M. J. Blaha, S. Dai, E. S. Ford, C. S. Fox, S. Franco *et al.*, "Heart disease and stroke statistics-2014 update," *Circulation*, vol. 129, no. 3, 2014.
- [59] P. R. Hoskins, "Physical properties of tissues relevant to arterial ultrasound imaging and blood velocity measurement," *Ultrasound in medicine & biology*, vol. 33, no. 10, pp. 1527–1539, 2007.
- [60] Y. Yuan and K. Shung, "Ultrasonic backscatter from flowing whole blood. i: Dependence on shear rate and hematocrit," *The Journal of the Acoustical Society of America*, vol. 84, no. 1, pp. 52–58, 1988.
- [61] X. Weng, G. Cloutier, P. Pibarot, and L.-G. Durand, "Comparison and simulation of different levels of erythrocyte aggregation with pig, horse, sheep, calf, and normal human blood," *Biorheology*, vol. 33, no. 4, pp. 365–377, 1996.
- [62] K. K. Shung, G. Cloutier, and C. C. Lim, "The effects of hematocrit, shear rate, and turbulence on ultrasonic Doppler spectrum from blood," *IEEE transactions on biomedical engineering*, vol. 39, no. 5, pp. 462–469, 1992.
- [63] S. Michaelson, "Health implications of exposure to radiofrequency/microwave energies," *Occupational and Environmental Medicine*, vol. 39, no. 2, pp. 105–119, 1982.
- [64] G. W. Stone, S. G. Ellis, A. Colombo, K. D. Dawkins, E. Grube, D. E. Cutlip, M. Friedman, D. S. Baim, and J. Koglin, "Offsetting impact of thrombosis and restenosis on the occurrence of death and myocardial infarction after paclitaxel-eluting and bare metal stent implantation," *Circulation*, vol. 115, no. 22, pp. 2842–2847, 2007.
- [65] P. Garg, D. J. Cohen, T. Gaziano, and L. Mauri, "Balancing the risks of restenosis and stent thrombosis in bare-metal versus drug-eluting stents: results of a decision analytic model," *Journal of the American College of Cardiology*, vol. 51, no. 19, pp. 1844–1853, 2008.
- [66] G. D. Dangas, B. E. Claessen, A. Caixeta, E. A. Sanidas, G. S. Mintz, and R. Mehran, "In-stent restenosis in the drug-eluting stent era," *Journal of the American College of Cardiology*, vol. 56, no. 23, pp. 1897–1907, 2010.
- [67] P. Sobieszczyk and A. Eisenhauer, "Management of patients after endovascular interventions for peripheral artery disease," *Circulation*, vol. 128, no. 7, pp. 749–757, 2013.

Supplementary Material for: Implantable Energy Harvesting Stents for Transcutaneous Wireless Monitoring of Peripheral Artery Disease

Michael A. Rothfuss Nicholas G. Franconi Kara N. Bocan Jignesh V. Unadkat Michael L. Gimbel Marlin H. Mickle Ervin Sejdić

I. MATERIALS AND METHODS

A. Deriving Anthropometric Simulation Models

1) *Skin, Fat, Muscle, and Bone*: In this work, the femur was modeled from cross-sectional slices of an average human male body [1], available from the NIH Visible Human Project [2], using the Visible Human Slice Viewer, available from École Polytechnique Fédérale de Lausanne [3]. The modeled femur length was 32 cm, beginning just below the femur head. The circumference is about 96 mm, which is at the upper range in American Caucasian men, $90.0 \text{ mm} \pm 5.9 \text{ mm}$, as reported by DiBennardo and Taylor [4], [5] via Steele and Bramblett [6].

Using anthropometric measurements, Bemben et al. modeled adipose and muscle layers as concentric circles to compute muscle cross-sectional area (CSA) as an alternative to the the gold standard, magnetic resonance imaging (MRI) [7]. $CSA = \pi(r - AT)^2$, where r is the mid-thigh radius, and AT is the average of the anterior and posterior mid-thigh adipose tissue thicknesses. We solved the CSA equation to approximate the muscle layer thickness. For young men, Bemben et al. reported an MRI-estimated CSA of $141.4 \pm 17.3 \text{ cm}^2$. A similar MRI-measured CSA was reported by Housh et al. for a similar age range [8]. Fuller et al. reported slightly lower MRI-measured CSA in elderly subjects in a cross-sectional slice slightly away from the mid-point of the thigh [9]; however, the range of Fuller et al.'s results are encompassed the data reported by Bemben et al. Solving for the mid-thigh muscle radius, $r - AT$, we get 6.3 cm to 7.1 cm ($\pm 1\sigma$). Thus, from the mid-shaft femur radius (15 mm) and the upper range of calculated mid-thigh muscle radius, the rectangular model muscle thickness is 56 mm.

Gibney et al. reported skin thickness and fat thicknesses in diabetics across a wide range of ages using ultrasound [10]. According to the study, both the 40–59 year old and ≥ 60 year old groups show a mean thigh skin thickness of 1.9 mm. This value was held constant in our simulations. As

for thigh fat thickness, Gibney et al. reported that age and fat thickness were not significantly related ($p = 0.45$). The mean thigh fat thicknesses were 10.4 mm and 10.3 mm for the two age ranges, respectively. However, because of the varied association of obesity with PAD (i.e., depending on the metric used), a range of fat thicknesses was used. For the entire male and female population, the range of fat thicknesses in the thigh from Gibney et al.'s work appears to be 1–31 mm, which was the range used for simulations in this paper.

2) *Vasculature and Atherosclerosis*: The femoral artery is the major supplier of blood to the legs. The superficial femoral artery (SFA), a continuation of the femoral artery distal to the profunda femoris branch, is the most common location for stenting in the lower limbs [11]. Specifically, the SFA segment in the adductor canal is the most common lesion location in the lower extremities [12]. The mean SFA outer diameter is $6.7 \pm 0.3 \text{ mm}$ (i.e., range 5.9 mm to 8.2 mm) [13], and the mean femoral artery wall thickness is $1.35 \pm 0.26 \text{ mm}$ [14]. We modeled the artery as one long straight segment of blood vessel tissue occupying nearly the length of the thigh model. Baskar et al. showed that the saphenous nerve, which is adjacent to the SFA, in the adductor canal lies at a depth of $27 \pm 6 \text{ mm}$ below the skin layer within the muscle [15]. For a mean fat thickness (10.4 mm) and skin thickness (1.9 mm), the mean SFA depth below the fat-muscle boundary can be approximated at $14.7 \pm 6 \text{ mm}$. The location of the vessel beneath fat-muscle boundary is set to 14.7 mm (i.e., from the vessel's top edge) and its location is varied across a 12 mm range (i.e., $\pm 6 \text{ mm}$).

The Trans-Atlantic Inter-Society Consensus for the Management of Peripheral Arterial Disease classifies femoral popliteal lesions by type [16], which vary widely, e.g., Type A: $\leq 5 \text{ cm}$ and Type D: $> 20 \text{ cm}$. Because plaque thickness was shown to affect implant turn-on power [17], the plaque thickness was simulated at three severity levels by varying the plaque wall thickness at 0 mm, 2.25 mm, and 4.5 mm, corresponding to 0% (i.e., after initial stent deployment), 50%, and 100% occlusion levels, respectively. Lumen renarrowing $\geq 50\%$ is a common metric used for PAD study inclusion criteria [18], [19] and represents an intermediate severity case. The complex plaque morphology was previously modeled as fat tissue by Daschner et al., which we followed in our simulations [20].

Michael A. Rothfuss, Nicholas G. Franconi, Kara N. Bocan, Marlin H. Mickle, and Ervin Sejdić are with the Department of Electrical and Computer Engineering, Swanson School of Engineering, University of Pittsburgh, Pittsburgh, PA, USA. E-mails: mar28@pitt.edu, ngf3@pitt.edu, knb12@pitt.edu, mickle@pitt.edu, esejdic@ieee.org

Jignesh V. Unadkat and Michael L. Gimbel are with the Department of Plastic Surgery, University of Pittsburgh, Pittsburgh, PA, USA. E-mails: unadkatjv@upmc.edu, gimbelml@upmc.edu.

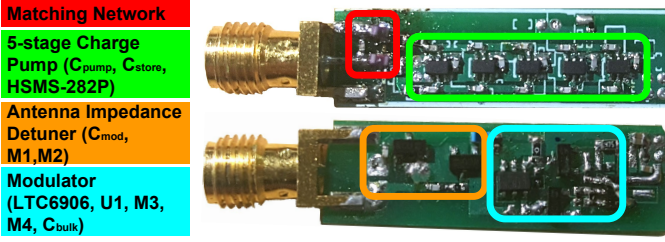


Fig. 1. Implanted electronics PCB showing its component sections.

B. Detailed Electronics Descriptions

1) *Implanted Rectifier & Modulator*: The implanted electronics are comprised of a five-stage fully differential Cockcroft-Walton voltage multiplier to convert the AC power at the implanted stent antenna terminals to a DC voltage, V_{rect} , to supply the load. A similar Cockcroft-Walton rectifier configuration was used with stent antennas by Chow et al. to power a cardiovascular pressure monitor at 3.7 GHz [21]. The load is a voltage-controlled oscillator (VCO) (LTC6906, Linear Technology, Milpitas, CA) with a square wave output and about a 2.25 V turn-on voltage. The square wave fundamental frequency, f_{osc} , is set by the current drawn from the VCO's *SET* pin. The *SET* pin current is proportional to V_{rect} and set by an op-amp, *U1*, and nMOS device, *M3*, in a constant-current source configuration. A voltage divider and level shifter, *M4*, set the current-source control voltage. The VCO's square wave output switches on the antenna impedance detuner, which is comprised of devices *M1*, *M2*, and modulating capacitors, C_{mod} . All MOSFETS are n-channel type devices (NX3020NAK, from NXP, Eindhoven, Netherlands), and all diodes are Schottky barrier diodes (HSMS-282P, from Avago Technologies, San Jose, CA, USA); the op-amp is an LT6003 (LTC6906, Linear Technology, Milpitas, CA).

Conjugate impedance matching the charge pump input port with the "Matching Network" in Figure 1 results in the minimum power required to achieve a V_{rect} [22]. The input impedance of the Cockcroft-Walton rectifier is non-linear because of the large signal behavior of the charge pump diodes. Impedance matching is performed at the steady-state impedance. The steady-state behavior of the rectifier, the expected simulation time needed to achieve steady-state for impedance matching, and a comparison of simulation and VNA measurements are shown in Figure 2. Close agreement between the simulated and measured rectifier input impedances is crucial for the full system simulations, where the tissue is modeled using lumped elements.

To characterize the implanted electronics, an Agilent 8753ES VNA and an oscilloscope are used to measure the VNA drive power versus the modulator frequency across the VCO's full output range (i.e., 30 kHz–1 MHz). The implanted electronics are impedance matched to the VNA's 50 Ω port impedance.

Figure 2 demonstrates the accuracy of the LTSpice simulator compared with VNA measurements for the purpose of designing impedance matching networks at the implanted electronics. The non-linear input impedance of the 5-stage

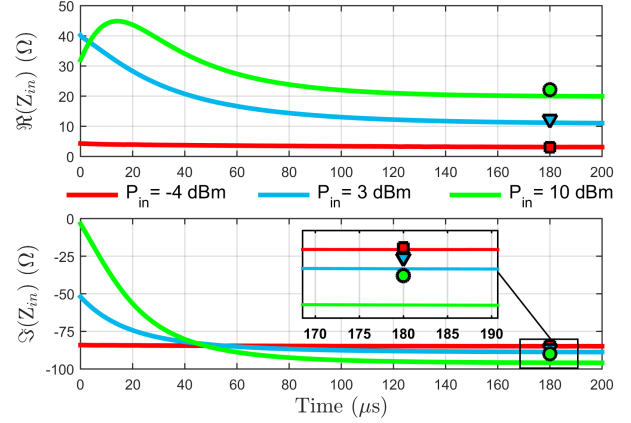


Fig. 2. A 5-stage Cockcroft-Walton rectifier with an 18 k Ω (meas.: 17.980 k Ω) static load at 315 MHz. Simulated $\Re(Z_{in})$ and $\Im(Z_{in})$ over time using the Pellerano et al. method [23]. Measured VNA data shown as points at 180 μ s for visualization only.

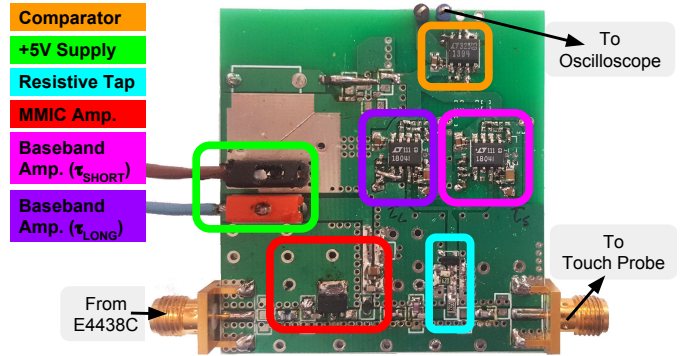


Fig. 3. Touch probe driver and demodulator PCB showing its component sections.

Cockcroft-Walton charge pump motivates the need to determine when the simulated steady-state impedances occur and how close they are to the steady-state measured values. In the figure, the simulated steady-state values begin at about 200 μ s. At 200 μ s, $\Re(Z_{in})$ is within 5.0% of the final simulated value and $\Im(Z_{in})$ is within 0.2% of the final simulated value. The final value is at 1000 μ s. The $\Re(Z_{in})$ percent-deviation from the final simulated value for $P_{in} = \{-4, 3, 10\}$ dBm is -5.0%, -2.3%, and -0.56%, respectively. At 1000 μ s, the measured-to-simulated $\Re(Z_{in})$ absolute error for the same P_{in} is 0.038 Ω , 1.5 Ω , and 2.3 Ω , respectively, while for $\Im(Z_{in})$, the absolute error is $j0.54 \Omega$, $j2.4 \Omega$, and $j6.0 \Omega$, respectively. Thus, we can conclude longer simulation times are necessary for smaller input drive powers, and larger drive powers increase the measurement-to-simulation impedance errors.

2) *External Touch Probe Driver & Demodulator*: Figure 3 illustrates the touch probe driver and demodulator. The gain block (MAAM-009560, by MACOM, Lowell, MA, USA) power gain and output-referred 1-dB compression point, about 15.6 dB and 24.16 dBm, respectively, were both measured on the PCB at 315 MHz in Figure 4.

The demodulator consists of a 20 dB resistive tap coupler, a diode demodulator, two baseband bandpass gain stages, and a

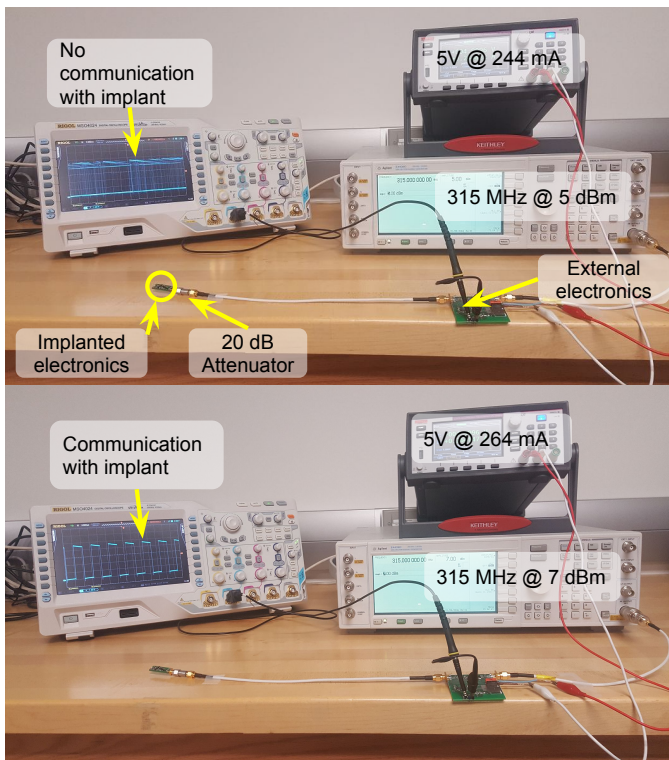


Fig. 4. Measurement set-up for received power at the implant with a 20 dB attenuator tissue surrogate.

comparator stage. One of the two baseband stages has a short time constant while the other has a long time constant. The short time-constant stage's simulated midband voltage gain is 80.6 dB at 318.9 kHz, and its half-voltage points are 99.2 kHz, 996.1 kHz, while for the long time-constant stage, 62.9dB at 120.9 kHz and 39.0 kHz 368.1 kHz. The long time-constant stage drives the comparator's reference level.

Shown Figure 4, the external driver electronics and the implanted electronics were tested for functionality using a tissue surrogate, an in-line bidirectional 2 Watt 20 dB attenuator (P/N: PE7001-20, Pasternack Enterprises, Irvine, CA, USA). An Agilent E4438C vector signal generator (VSG) drives the external driver PCB input port. When the VSG drive level is insufficient to turn on the implant, the comparator output transitions erratically. When the implant turns on, the implant's VCO frequency is recovered and visible on the oscilloscope. Because the implant will be impedance matched while implanted, similarly, this set-up matches the implanted electronics to 50 Ω , the characteristic impedance of the surrogate – the 20 dB attenuator.

II. RESULTS

A. Electronics Benchmarking

Figure 5 shows both simulated and measured modulation frequency for a given input power for the unmatched and matched impedance cases when driven by a 50 Ω source. The simulated and measured results show good agreement. The importance of impedance matching the implant to the driving source (i.e., in this figure, the 50 Ω VNA source) is

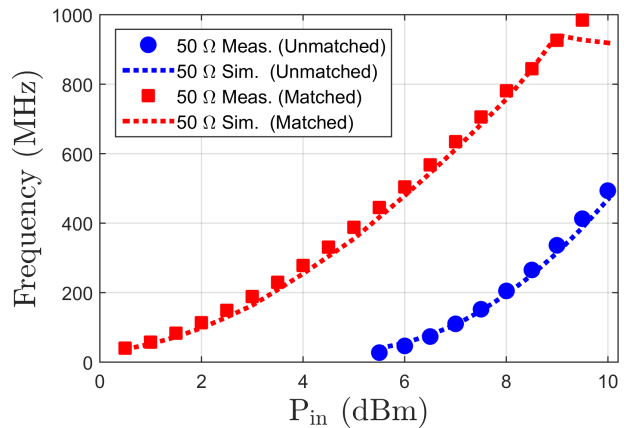


Fig. 5. Simulated and measured implant modulation frequency for a given input power. Both matched and unmatched cases use a 50 Ω source impedance.

evident – the turn on power in the unmatched case is 5.5 dBm, while the turn on power in the matched case is 0.5 dBm. The matched case exploits nearly the full-range of the VCO's output frequency, compared with the unmatched case's 494 kHz maximum output frequency. Also, considering the power gain and output-referred compression point of the PA, the unmatched case will severely limit the maximum depth for viable communication with the implant. Additionally, the figure shows that input powers greater than 9 dBm show significant errors for the simulated match case compared to the measured, and therefore, simulated power drives should remain below this level.

Figure 6 serves to benchmark the external driver and demodulator with respect to a practical *well-defined* loss network – a 20 dB attenuator. The figure shows the measured power levels, at the output of a measured 20.27 dB attenuator, on a E4443A spectrum analyzer (SA) and received power at the implant corresponding to the demodulated frequency viewed on an oscilloscope. The absolute error between the two measurements is also shown. The turn-on power of the implant electronics occurs at 1.07 dBm for a measured 22.04 dBm available at the external driver port and 1.77 dBm available into a matched load after the 20.27 dB attenuator. The results demonstrate operation of the implant through a representative attenuation environment. The maximum available power from the external driver is 24.67 dBm. Therefore, the maximum permissible tissue attenuation is 24.17 dB, for an impedance matched implant with a turn-on power threshold of 0.5 dBm as shown in Figure 5.

REFERENCES

- [1] M. Bleeker, *Anatomy Live: Performance and the operating theatre*. Amsterdam University Press, 2008, vol. 1.
- [2] "The National Library of Medicines Visible Human Project," http://www.nlm.nih.gov/research/visible/visible_human.html, accessed: 2015-03-06.
- [3] Peripheral Systems Lab at the École Polytechnique Fédérale de Lausanne, "Visible Human Server: Slice, surface and animation server," <http://visiblehuman.epfl.ch/stdapplelv2.php>, accessed: 2015-03-06.
- [4] R. DiBennardo and J. V. Taylor, "Sex assessment of the femur: a test of a new method," *American Journal of Physical Anthropology*, vol. 50, no. 4, pp. 635–637, 1979.

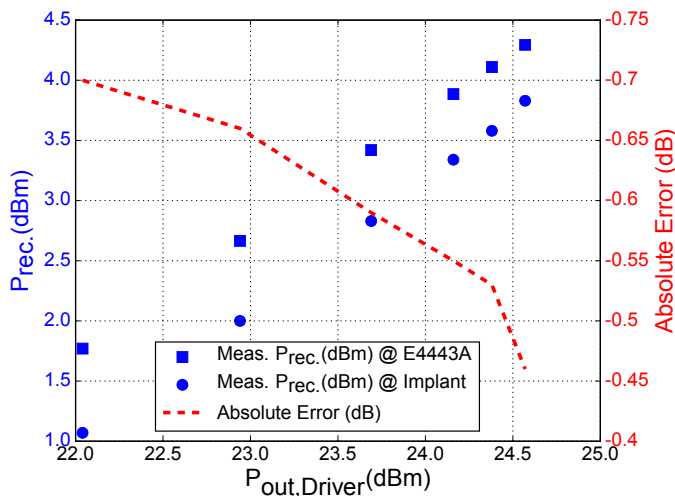


Fig. 6. Measured power on the E4443A SA and the implanted electronics for a given PA output power, $P_{out,PA}$, through a measured measured to be 20.27 dB attenuator.

[5] R. Dibennardo and J. V. Taylor, "Classification and misclassification in sexing the black femur by discriminant function analysis," *American Journal of Physical Anthropology*, vol. 58, no. 2, pp. 145–151, 1982.

[6] D. G. Steele, *The anatomy and biology of the human skeleton*. Texas A&M University Press, 1988.

[7] M. G. Bembem, Y. Sato, and T. Abe, "The use of anthropometry for assessing muscle size," *International Journal of KAATSU Training Research*, vol. 1, no. 1, pp. 33–36, 2005.

[8] D. J. Housh, T. J. Housh, J. P. Weir, L. L. Weir, G. O. Johnson, and J. R. Stout, "Anthropometric estimation of thigh muscle cross-sectional area," *Medicine and Science in Sports and Exercise*, no. 27, pp. 784–91, 1995.

[9] N. Fuller, C. Hardingham, M. Graves, N. Screaton, A. Dixon, L. Ward, and M. Elia, "Predicting composition of leg sections with anthropometry and bioelectrical impedance analysis, using magnetic resonance imaging as reference," *Clinical Science*, vol. 96, pp. 647–657, 1999.

[10] M. A. Gibney, C. H. Arce, K. J. Byron, and L. J. Hirsch, "Skin and subcutaneous adipose layer thickness in adults with diabetes at sites used for insulin injections: implications for needle length recommendations," *Current Medical Research and Opinion*, vol. 26, no. 6, pp. 1519–1530, 2010.

[11] M. M. Chowdhury, A. D. McLain, and C. P. Twine, "Angioplasty versus bare metal stenting for superficial femoral artery lesions," *The Cochrane Library*, 2014.

[12] P. H. Arger, *The complete guide to vascular ultrasound*. Lippincott Williams & Wilkins, 2004.

[13] G. Rådegran and B. Saltin, "Human femoral artery diameter in relation to knee extensor muscle mass, peak blood flow, and oxygen uptake," *American Journal of Physiology-Heart and Circulatory Physiology*, vol. 278, no. 1, pp. H162–H167, 2000.

[14] M. Wong, J. Edelstein, J. Wollman, and M. G. Bond, "Ultrasonographic comparison of the human arterial wall: Verification of intima-media thickness," *Arteriosclerosis, Thrombosis, and Vascular Biology*, vol. 13, no. 4, pp. 482–486, 1993.

[15] B. Manickam, A. Perlas, E. Duggan, R. Brull, V. W. Chan, and R. Ramlogan, "Feasibility and efficacy of ultrasound-guided block of the saphenous nerve in the adductor canal," *Regional anesthesia and pain medicine*, vol. 34, no. 6, pp. 578–580, 2009.

[16] L. Norgren, W. R. Hiatt, J. A. Dormandy, M. R. Nehler, K. A. Harris, F. G. R. Fowkes, and TASC II Working Group and others, "Inter-society consensus for the management of peripheral arterial disease (TASC II)," *European Journal of Vascular and Endovascular Surgery*, vol. 33, no. 1, pp. S1–S75, 2007.

[17] C. Occhiuzzi, G. Contri, and G. Marrocco, "Design of implanted RFID tags for passive sensing of human body: the STENTag," *IEEE Transactions on Antennas and Propagation*, vol. 60, no. 7, pp. 3146–3154, 2012.

[18] J. Lammer, M. Bosiers, T. Zeller, M. Schillinger, E. Boone, M. J. Zaugg, P. Verta, L. Peng, X. Gao, and L. B. Schwartz, "First clinical

trial of nitinol self-expanding everolimus-eluting stent implantation for peripheral arterial occlusive disease," *Journal of vascular surgery*, vol. 54, no. 2, pp. 394–401, 2011.

[19] M. Bosiers, G. Torsello, H.-M. Giffler, J. Ruef, S. Müller-Hülsbeck, T. Jahnke, P. Peeters, K. Daenens, J. Lammer, H. Schroë *et al.*, "Nitinol stent implantation in long superficial femoral artery lesions: 12-month results of the durability i study," *Journal of Endovascular Therapy*, vol. 16, no. 3, pp. 261–269, 2009.

[20] F. Daschner, S. Hoffmann, R. Knochel, M. Jerosch-Herold, and C. Rickers, "Resonant stents for non-invasive monitoring of restenosis," in *2011 41st European Microwave Conference*. IEEE, 2011, pp. 972–975.

[21] E. Y. Chow, A. L. Chlebowski, S. Chakraborty, W. J. Chappell, and P. P. Irazoqui, "Fully wireless implantable cardiovascular pressure monitor integrated with a medical stent," *IEEE Transactions on Biomedical Engineering*, vol. 57, no. 6, pp. 1487–1496, 2010.

[22] M. Stoopman, S. Keyrouz, H. J. Visser, K. Philips, and W. A. Serdijn, "Co-design of a CMOS rectifier and small loop antenna for highly sensitive RF energy harvesters," *IEEE Journal of Solid-State Circuits*, vol. 49, no. 3, pp. 622–634, 2014.

[23] S. Pellerano, J. Alvarado Jr, and Y. Palaskas, "A mm-wave power-harvesting RFID tag in 90 nm CMOS," *IEEE Journal of Solid-State Circuits*, vol. 45, no. 8, pp. 1627–1637, 2010.